AGU PUBLICATIONS

JGR

Journal of Geophysical Research: Earth Surface

RESEARCH ARTICLE
10.1002/2015JF003806

Key Points:
- Radar basal reflectivity in a grounding zone embayment is lower than that expected from an ice-seawater interface
- Radar amplitude and waveform modeling suggests that basal reflectivity is reduced by entrained sediment and basal roughness
- A reflectivity increase downflow of the grounding line suggests that sediment deposition in grounding zones occurs via basal debris melt-out

Correspondence to:
K. Christianson,
knut@uw.edu

Citation:
Christianson, K., R. W. Jacobel, H. J. Horgan, R. B. Alley, S. Anandakrishnan, D. M. Holland, and K. J. DallaSanta (2016), Basal conditions at the grounding zone of Whillans Ice Stream, West Antarctica, from ice-penetrating radar, *J. Geophys. Res. Earth Surf.*, *121*, 1954–1983, doi:10.1002/2015JF003806.

Received 11 DEC 2015
Accepted 22 SEP 2016
Accepted article online 1 OCT 2016
Published online 4 NOV 2016

©2016. American Geophysical Union. All Rights Reserved.

Basal conditions at the grounding zone of Whillans Ice Stream, West Antarctica, from ice-penetrating radar

Knut Christianson[1], Robert W. Jacobel[2], Huw J. Horgan[3], Richard B. Alley[4], Sridhar Anandakrishnan[4], David M. Holland[5], and Kevin J. DallaSanta[5]

[1]Department of Earth and Space Sciences, University of Washington, Seattle, Washington, USA, [2]Physics Department, Saint Olaf College, Northfield, Minnesota, USA, [3]Antarctic Research Centre, Victoria University of Wellington, Wellington, New Zealand, [4]Department of Geosciences and Earth and Environmental Systems Institute, Pennsylvania State University, University Park, Pennsylvania, USA, [5]Courant Institute of Mathematical Sciences, New York University, New York, New York, USA

Abstract We present a comprehensive ice-penetrating radar survey of a subglacial embayment and adjacent peninsula along the grounding zone of Whillans Ice Stream, West Antarctica. Through basal waveform and reflectivity analysis, we identify four distinct basal interfaces: (1) an ice-water-saturated till interface inland of grounding; (2) a complex interface in the grounding zone with variations in reflectivity and waveforms caused by reflections from fluting, sediment deposits, and crevasses; (3) an interface of anomalously low-reflectivity downstream of grounding in unambiguously floating areas of the embayment due to basal roughness and entrained debris; and (4) a high-reflectivity ice-seawater interface that occurs immediately seaward of grounding at the subglacial peninsula and several kilometers seaward of grounding in the embayment, occurring after basal debris and grounding zone flutes have melted off the ice bottom. Sediment deposition via basal debris melt-out occurs in both locations. The higher basal melt rate at the peninsula contributes to greater grounding line stability by enabling faster construction of a stabilizing sediment wedge. In the embayment, the low slopes of the ice bottom and bed prevent development of a strong thermohaline circulation leading to a lower basal melt rate and less rapid sediment deposition. Thus, grounding lines in subglacial embayments are more likely to lack stabilizing sediment deposits and are more prone to external forcing, whether from the ocean, the subglacial water system, or large-scale ice dynamics. Our conclusions indicate that subglacial peninsulas and embayments should be treated differently in ice sheet-ocean models if these models are to accurately simulate grounding line response to external forcing.

1. Introduction

Weertman [1974] proposed the marine ice sheet instability more than 40 years ago. This hypothesis states that retreat of an ice sheet grounded well below sea level on a reverse-sloping bed should continue unless stabilized by other factors. Since that time, critical advances have been made in locating and mapping grounding zones using remote sensing [*Gray et al.*, 2002; *Horgan and Anandakrishnan*, 2006; *Fricker et al.*, 2009; *Brunt et al.*, 2010; *Rignot et al.*, 2011], incorporating theoretical descriptions of grounding zones into ice sheet models [*Schoof*, 2007; *Nowicki and Wingham*, 2008; *Parizek and Walker*, 2010; *Parizek et al.*, 2013], and reconstructing paleo grounding zone positions [*Anderson et al.*, 2002; *Alley et al.*, 1989; *Dowdeswell and Fugelli*, 2012]. But due to the inherent inaccessibility of modern grounding zones, field observations remain scarce and are limited to just a few locations [e.g., *Smith*, 1996; *Anandakrishnan et al.*, 2007; *MacGregor et al.*, 2011; *Horgan et al.*, 2013a, 2013b; *Christianson et al.*, 2013]. Lack of critical observations of (de)stabilizing mechanisms in grounding zones, such as grounding zone sedimentation and ice-ocean interactions, limits our ability to accurately model grounding zones and thus also ice sheet evolution.

The physical nature of ice-ocean interactions in grounding zones, and how they control the magnitude of subice shelf melting and thus impact ice flow speed, is important but poorly understood [e.g., *Jenkins and Doake*, 1991; *Holland and Jenkins*, 1999; *Holland et al.*, 2008; *Walker et al.*, 2009; *Jenkins*, 2011]. For example, recent observations indicate that large (kilometer scale) subglacial channels are common beneath ice shelves [*Jenkins et al.*, 2010; *Dutrieux et al.*, 2013; *Stanton et al.*, 2013; *Le Brocq et al.*, 2013; *Langley et al.*, 2014; *Alley et al.*, 2016; *Marsh et al.*, 2016]. Modeling indicates that these channels may align with modeled meltwater pathways

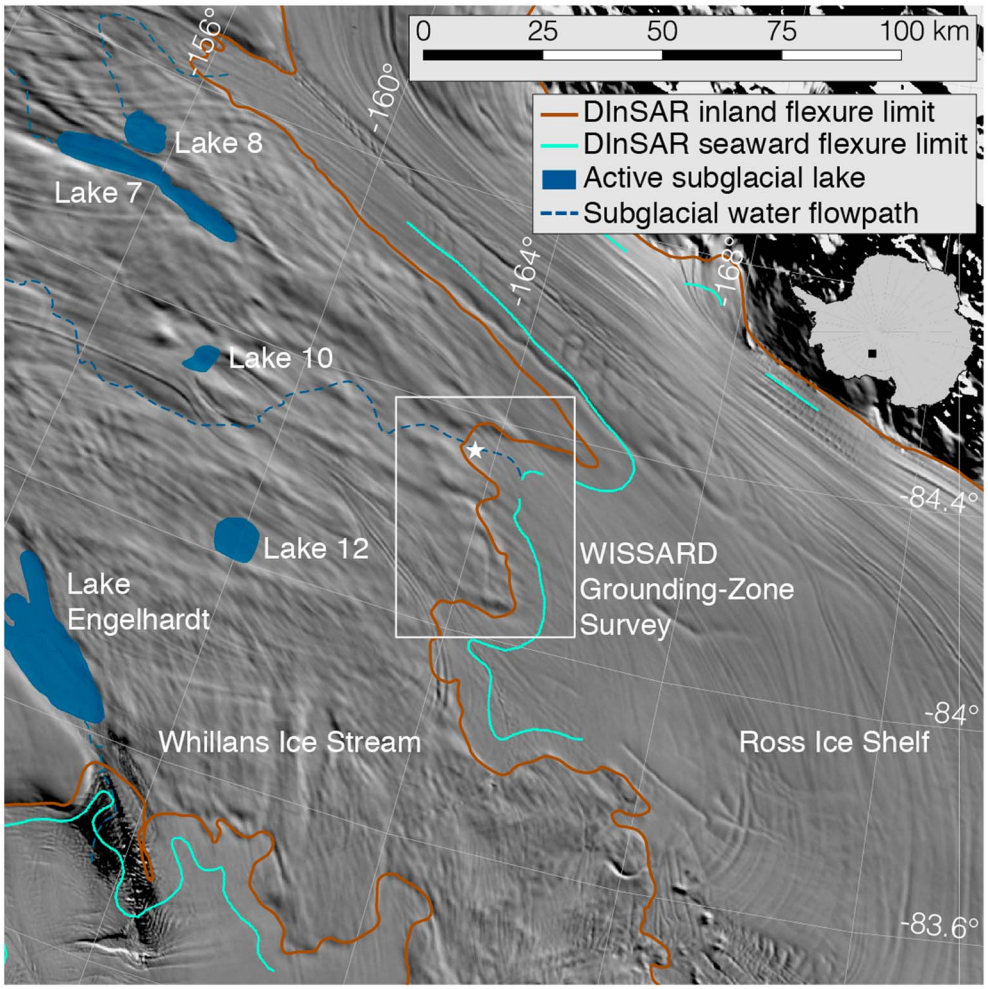

Figure 1. Locator map of Whillans Ice Stream highlighting the area of the grounding zone survey (white box). Inset shows location within Antarctica. White star indicates the drill site for the WISSARD project. Subglacial lake extents and subglacial water flow paths are from *Fricker and Scambos* [2009] and *Carter and Fricker* [2012]. Grounding lines are from *Rignot et al.* [2011] and *Depoorter et al.* [2014]. Background imagery is Moderate Resolution Imaging Spectroradiometer (MODIS) MOA [*Haran et al.*, 2005]

beneath the grounded ice sheet [*Le Brocq et al.*, 2013; *Marsh et al.*, 2016] and are therefore likely to impact grounding zone basal melt rates [*Jenkins*, 2011]. However, the location of highest basal melt rate is unclear, with some studies indicating greatest melt at channel apexes [*Stanton et al.*, 2013], while other studies suggest enhanced melt at channel keels [*Dutrieux et al.*, 2013], and a real possibility that the locus of greatest melt can change over time or space. As basal melt rate variation significantly affects both ice shelf mass balance [*Prtichard et al.*, 2012; *Millgate et al.*, 2013] and buoyant meltwater plume dynamics [*Jenkins and Doake*, 1991; *Holland and Jenkins*, 1999; *Jenkins*, 2011; *Gladish et al.*, 2012], knowledge of subice shelf oceanography and its effects on grounding zone stability is likely inadequate in the current generation of coupled ice-ocean models. Furthermore, while these recent observations imply channelized subglacial water routing beneath ice shelves, the dominance of this mode of meltwater routing is unclear, especially its upstream continuation under the grounded ice sheet, where the distribution of subglacial water may have direct influence on ice flow velocities [e.g., *Anandakrishnan and Alley*, 1997; *Creyts and Schoof*, 2009; *Carter et al.*, 2013; *Siegfried et al.*, 2016]. Melt at the grounding zone is additionally important as it results in sediment deposition due to the raining out of englacial debris. These deposits contribute to the grounding zone wedges that are observed on the continental shelf surrounding Greenland and Antarctica [*Christoffersen et al.*, 2010; *Dowdeswell and Fugelli*, 2012; *Anderson et al.*, 2002] and are thought to stabilize the grounding zone position against small changes in sea level or ice thickness [*Alley et al.*, 2007].

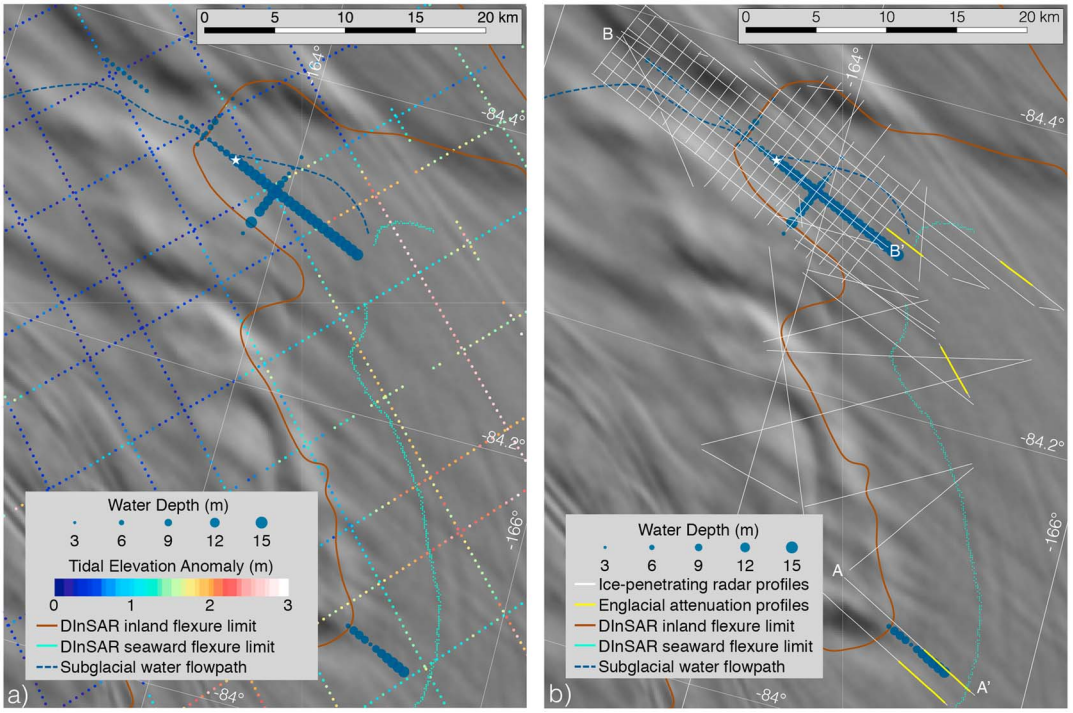

Figure 2. Ground-based radar survey at the Whillans Ice Stream grounding zone. (a) Tidal elevation anomaly (surface elevation range throughout the ICESat period; see *Smith et al.* [2009] and *Horgan et al.* [2012] for processing methodology) and ocean water depth from seismic data [*Horgan et al.*, 2013a] in study area and (b) radar survey lines. In Figure 2b, five profile segments used to calculate englacial attenuation rate are highlighted in yellow, and profiles used in subsequent figures are labeled. White star indicates the drill site for the WISSARD project. Subglacial water flow path is from *Carter and Fricker* [2012]. Grounding lines are from *Rignot et al.* [2011] and *Depoorter et al.* [2014]. Background imagery is MODIS MOA [*Haran et al.*, 2005].

Table 1. Dielectric Properties of Common Subglacial Materials for a 5 MHz Radar Wave[a]

Material	Permittivity	Conductivity (S m^{-1})	Power Reflectivity (dB)	Attenuation (dB/μs)
Glacier ice[b]	3.2	7.0×10^{-5}	N/A	−21.5
Marine ice[c]	3.4	5.7×10^{-4}	−18	−164
Groundwater ice[d]	3.2	6.6×10^{-4}	−16	−203
Debris-laden ice (15% sand)[e]	3.1	8.0×10^{-5}	−41	−25.3
Seawater[f]	77	2.9	−0.22	−∞
Freshwater[g]	80	1.0×10^{-4}	−3.5	−1.23
Groundwater[h]	80	0.37	−0.64	−~10^3
Sand[h]	2.6	1.3×10^{-4}	−25	−49.1
Groundwater till (40% gw)[i]	36	0.037	−2.2	−1000
Freshwater till (15–45% fw)[i]	6 to 20	2.0×10^{-4} to 3.0×10^{-4}	−7.4 to −16	−14.6 to −31.9
Frozen till (40% gw ice)[i]	2.9	3.4×10^{-4}	−22	−116
Frozen bedrock (15% gw ice)[i]	2.7	2.0×10^{-4}	−25	−71.3
Unfrozen bedrock (15% gw)[i]	12	0.0048	−6.2	−390

[a]Basal reflectivities assume a specular interface that consists of clean glacier ice and the substrate material.
[b]*Smith and Evans* [1972], *Glen and Paren* [1975], *Neal* [1979], *Peters et al.* [2005], and *MacGregor et al.* [2007].
[c]*Neal* [1979] and *Peters et al.* [2005].
[d]*Peters et al.* [2005].
[e]Looyenga's dielectric mixing formula [*Looyenga*, 1965] was used.
[f]*Hasted* [1961], *Smith and Evans* [1972], *Neal* [1979], and *Ellison et al.* [1998].
[g]*Boithias* [1987] and *Peters et al.* [2005].
[h]*Keller* [1966] and *Peters et al.* [2005].
[i]Looyenga's dielectric mixing formula [*Looyenga*, 1965] with sand was used.

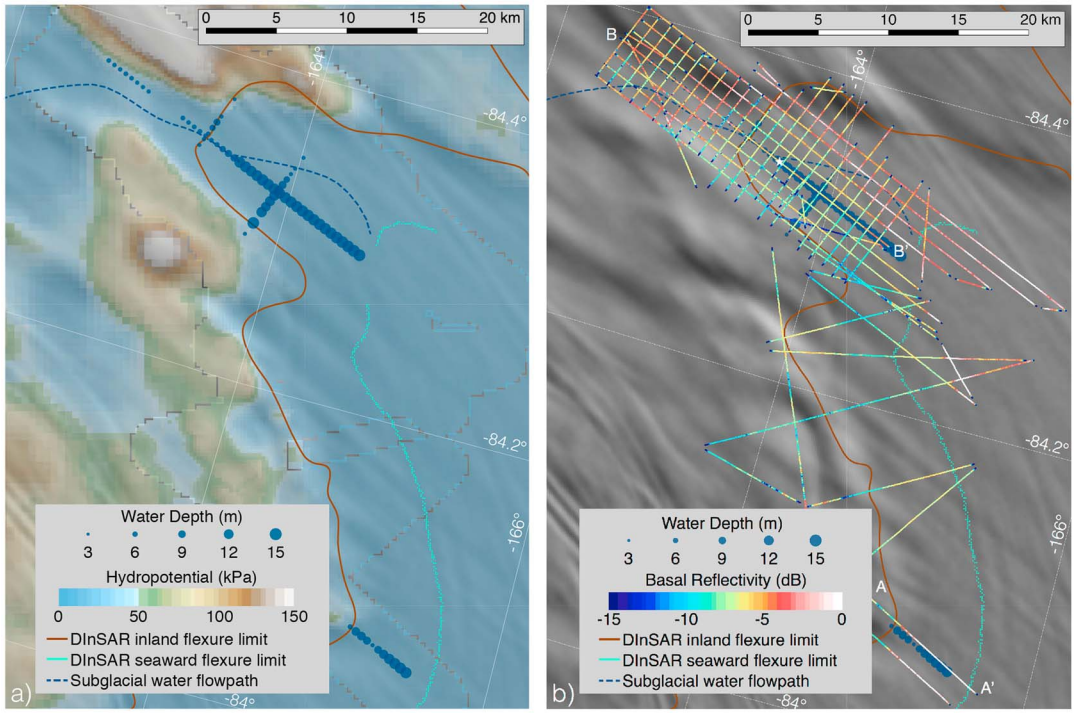

Figure 3. (a) Hydropotential and (b) radar basal reflectivity at the Whillans Ice Stream grounding zone. Ocean water column depths [*Horgan et al.*, 2013a, 2013b] are indicated by blue circles. White star indicates the drill site for the WISSARD project. Subglacial water flow path is from *Carter and Fricker* [2012]. Grounding lines are from *Rignot et al.* [2011] and *Depoorter et al.* [2014]. Background imagery is MODIS MOA [*Haran et al.*, 2005].

Here we focus on ice-penetrating radar observations of the ice internal stratigraphy, grounding zone geometry, and physical nature of the ice-bottom interface in a subglacial embayment and an adjacent peninsula of the Whillans Ice Stream grounding zone (Figures 1 and 2). We focus especially on basal reflectivity because it is particularly sensitive to basal properties, and in the subglacial embayment, as in other surveys along the Siple Coast [e.g., *Anandakrishnan et al.*, 2007; *MacGregor et al.*, 2011], reflectivity over floating ice is anomalously low compared to the expected reflectivity from an ice-seawater interface (see Table 1 and Figures 3 and 4). Our aim is to understand the roles of subglacial sediments, subglacial melt water, local oceanography, and their influences on grounding zone stability.

2. Background

During the 2011–2012 austral summer (early December to mid-January), we completed a comprehensive geophysical survey of the grounding zone of Whillans Ice Stream, West Antarctica. We conducted active-source seismic [*Horgan et al.*, 2013a, 2013b], ice-penetrating radar and kinematic GPS [*Christianson et al.*, 2013], and gravity surveys [*Muto et al.*, 2013] at the modern grounding zone of Whillans Ice Stream, West Antarctica (Figures 1 and 2). Our surveys targeted two distinct subglacial environments: an embayment where several subglacial lakes are suspected to drain [*Carter and Fricker*, 2012; *Le Brocq et al.*, 2013] and a nearby peninsula where vigorous drainage is unlikely (Figure 2) [*Carter and Fricker*, 2012; *Le Brocq et al.*, 2013]. At the peninsula (line AA′ in Figure 2), the present grounding zone flotation point is located at a small bathymetric bump that is probably sediment controlled [*Horgan et al.*, 2013a]. No local ice plain is present, and a relatively steep hydropotential gradient beneath the downstream most grounded ice (>50 kPa km^{-1}) makes extensive mixing of subglacial and ocean water unlikely [*Horgan et al.*, 2013a]. In the embayment (line BB′ in Figure 2), the ice ungrounds much more gradually, and there is a significant local ice plain where the ice is only ephemerally grounded. Beneath this ice plain, seismic data indicate that prograding sedimentation has occurred [*Horgan et al.*, 2013a]. There is also evidence of a bathymetric step that may be the active front of the sedimentary lobe. A broad hydropotential low extending upstream from the grounding zone opens into a transverse trough and eventually a large longitudinal subglacial channel

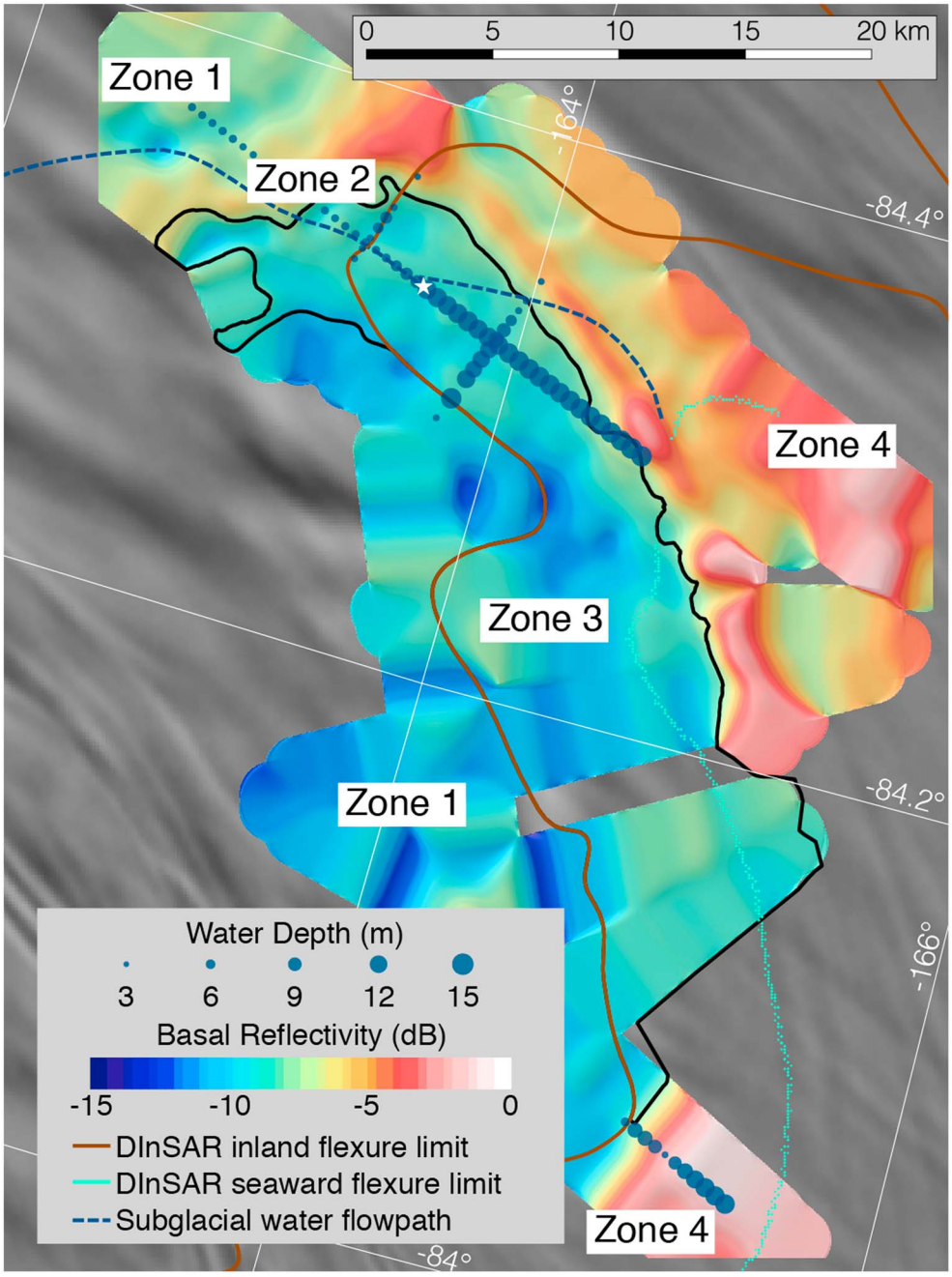

Figure 4. Gridded basal reflectivity after correcting for geometric spreading and englacial attenuation. Reflectivity categorizations 1 to 4 are discussed in the text. White star indicates the drill site for the WISSARD project.

(~1 km wide and ~7 m deep). The hydropotential gradient (20 to 30 kPa km^{-1}) along the trough axis in the grounding zone is low enough that calculations indicate it can be overcome by the tides, creating an extended zone of tidal influence where interaction of subglacial and ocean water is likely [*Horgan et al.*, 2013b]. There is no evidence in either location of a high-profile grounding zone sediment wedge similar to those found on the surrounding continental margin [cf. *Anderson et al.*, 2002]. However, folds in radar internal-reflecting horizons (IRHs) that are located just upstream of the grounding zone in both locations are likely formed due to resistance to flow of the ice over a zone of sediment that is compacted by ice sheet tidal flexure [*Christianson et al.*, 2013]. Modeling indicates that this process may stabilize grounding line position in the absence of positive topography [*Christianson et al.*, 2013].

3. Methods

3.1. Kinematic GPS

We collected over 1000 line kilometers of dual-frequency kinematic GPS profiles across the grounding zone to precisely locate our ice-penetrating radar data and obtain grounded and floating ice surface elevations. Moderate-rate (1 Hz) GPS data were collected with Trimble NetRS and NetR8 receivers and Trimble Zephyr Geodetic antennas. The rover antenna was mounted on a steel pole that extended ~10 cm above the radar shelter. Horizontal swaying was negligible due to slow driving speeds (~6–8 kph) and relatively low-amplitude sastrugi (≤50 cm). Although narrow strand cracks (a few centimeters wide at the surface) were observed in some areas near the grounding zone, no large, open crevasses were visible in the survey area. Rover data were processed kinematically relative to a local base station on fully grounded ice using differential carrier phase positioning with epoch-by-epoch zenith tropospheric delay estimation [*Chen*, 1998; *King*, 2004]. Base station coordinates were computed relative to a rock site (Ramsey Glacier) ~200 km from the local base station. Rover position uncertainties are 5 cm or less in all dimensions.

3.2. Ice-Penetrating Radar

3.2.1. System Characteristics

Ice-penetrating data were collected using an impulse radar system operating at a center frequency of ~5 MHz (λ_{ice} = 34 m). The system has undergone many changes over the years [*Welch and Jacobel*, 2003; *Welch et al.*, 2009; *Christianson et al.*, 2012], primarily improvements to the digitizer receiver to increase the dynamic range, stacking speed, and time resolution. For this project, we utilized a commercially made pulse generator produced by Kentech Instruments, operating at a 1 kHz pulse-repetition frequency with a pulse amplitude of 4 kV. The resistively tapered dipole antenna arms were each 10 m in length (20 m per pair), and the system was towed by snowmobile on two sleds with antenna center points separated by ~167 m. The large separation between the transmitter and receiver reduced the interference of the direct arrival (air wave) on the early arrivals from shallow depths. The digitizer receiver was a two-channel, 200 MHz, 14-bit digitizing PCI board made by GaGe Applied Electronics and housed in a ruggedized, military-grade computer. One channel digitized a low-gain signal and the other an amplified signal for higher gain. This board provides 84 dB of dynamic range for raw traces and a time accuracy of 5 ns, or approximately 0.5 m of ice thickness. Triggering for the digitizer was initiated by the air-wave arrival, and typically 1000 triggers were stacked (averaged) for each recorded waveform. At usual speeds of surface travel, this resulted in an average spacing of about 3 m per waveform.

We note that this type of impulse radar, with dipole antennas towed end to end, has significant gain from side lobes in the radiation pattern in the off-nadir directions, both fore and aft of the transmitter-receiver pair and to either side [*Engheta et al.*, 1982; *Arcone*, 1995; *Jacobel et al.*, 2014]. For example, *Arcone* [1995] showed that the antenna radiation pattern for a similar system has a gain only 3 dB less than the maximum at angles out to 25° from the nadir. This pattern of receptivity can produce strong returns from targets within the side lobes at arrival times greater than the nadir, mimicking targets that appear to be below the basal reflector, which complicates interpretation.

3.2.2. Radar Processing

Altogether we acquired ~700 line kilometers of radar data using the radar system described above (see section 3.2.1). Traces were geolocated using the time stamp recorded with the waveform from the GPS receiver, and positions were corrected to the midpoint between the transmitter and the receiver. Processing included band pass filtering (Butterworth band pass from 1 to 10 MHz), time correction for antenna separation, interpolation to a precise trace spacing of 3.0 m, and along-track time-wave number migration. Migration and conversion of travel time to depth assumed an average radar wave speed in ice of 169 m μs^{-1}. Surface elevation, bed elevation, internal layer topography, and glaciostatic hydropotential [*Shreve*, 1972] were derived from the RES and GPS data interpolated to a 10 m posting using the nearest-neighbor algorithm with a search radius of 1 km and then smoothed using a two-dimensional Gaussian filter with a 6σ width of 2.5 km. Gridding parameters were chosen to eliminate obvious artifacts. In all profiles, the basal reflection is clearly visible, and we frequently image IRHs to within a few meters of the basal reflection. The first multiple of the basal reflection is commonly detected, especially where the basal reflection is strong (Figure 5). The basal and multiple reflections, IRHs, and other prominent features in the radar data were digitized using a semi-automated routine that identified the Ricker wavelet corresponding to the selected reflection [*Gades et al.*, 2000]. The reflection power is calculated as the sum-of-the-squared amplitudes normalized by the number of samples between the two outer peaks of the identified Ricker wavelet (Appendix A).

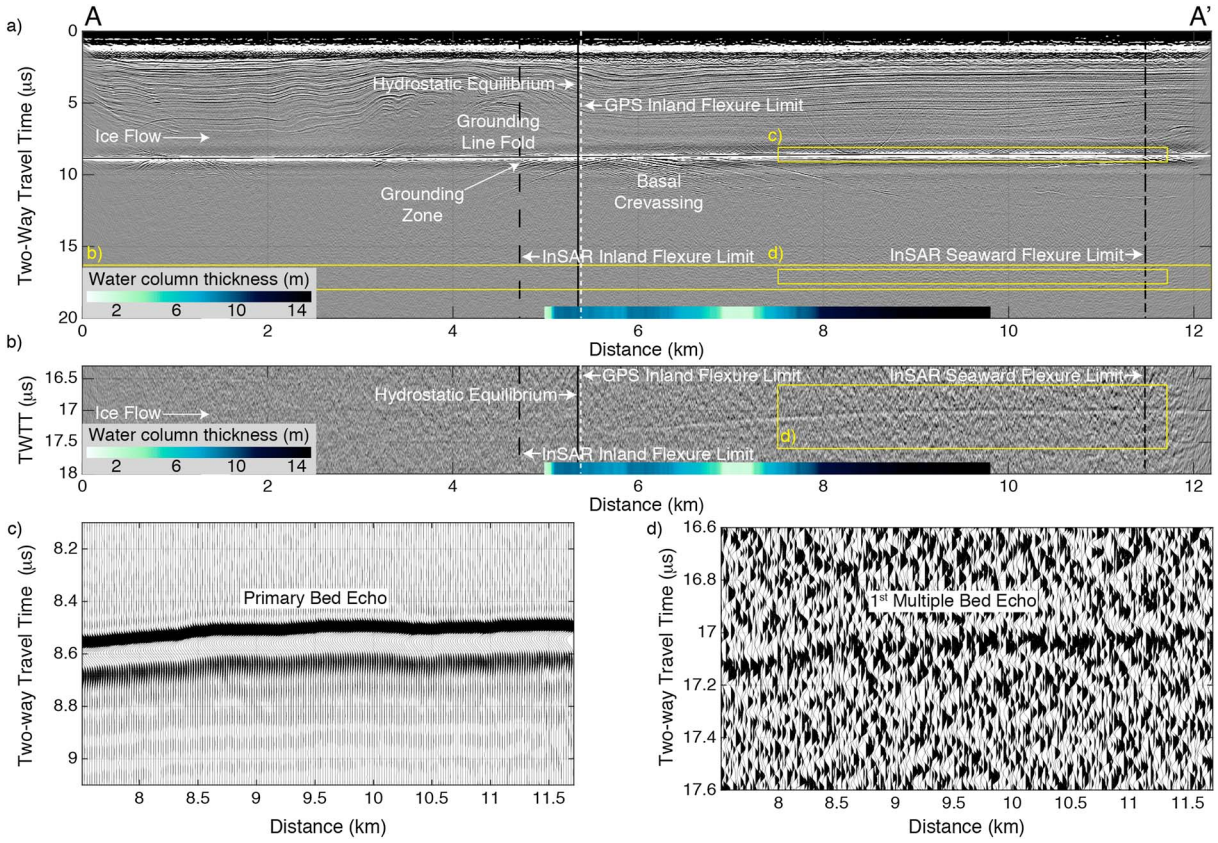

Figure 5. Observations of the primary bed reflection and the first multiple bed reflection for profile AA′ (see Figure 2b for location). (a) Radargram of profile AA′ showing the bed reflection and its first multiple. (b) Expansions of the first multiple of the bed reflection (marked in Figure 5a; visible from 6 km seaward). Variable area amplitude wiggle plots of (c) the bed reflection and (d) the first multiple wavelet in the boxes shown in Figure 5a where the ice-bed interface is unambiguously glacier ice-seawater. In Figures 5a and 5b, colorbar indicates depth of seismically imaged water column [*Horgan et al.*, 2013a] and grounding line metrics detected using InSAR, GPS, and hydrostatic calculations are shown [*Christianson et al.*, 2013].

3.2.3. Estimating Absolute Basal Reflectivity

To determine the reflection coefficient of the ice-bed interface, we applied geometric and attenuation corrections. Sufficiently far downglacier of the grounding zone (yellow profiles in Figure 2b), we find strong and consistent basal reflections and their first multiples (Figure 5), where it is expected that a smooth, specular interface separates clean ice from seawater. The reflection coefficient at the base and the upper surface of the ice can be calculated directly in this case, so the ratio of the first multiple of the basal reflection to the primary basal reflection yields the depth-averaged englacial attenuation rate [*MacGregor et al.*, 2011] (Appendix A). To select portions of radar profiles where the basal reflection is almost certainly from an ice-seawater interface, we require that the seismically imaged water column is at least 6 m thick, the ice is in full hydrostatic equilibrium, and the basal returned power is uniformly strong (Figure 2b and Appendix A). We identify 5925 traces spanning 17.76 line kilometers and 37.6 m ice thickness variation that satisfy these criteria. If we assume that the depth-averaged attenuation rate (N_a) is uniform over our relatively small survey area, the spatially averaged, one-way attenuation rate in this survey is $N_a = 17.8 \pm 2.1$ dB km^{-1} (Appendix A). This value is comparable to results from other studies in this region [*Peters et al.*, 2005; *Jacobel et al.*, 2009; *MacGregor et al.*, 2011] but is significantly greater than attenuation rates in overall colder ice columns [*Oswald and Gogineni*, 2008; *Jacobel et al.*, 2010; *Christianson et al.*, 2014]. We note that basal debris load is likely negligible in the areas used in this calculation; there are no point diffractors, areas of dim or variable reflectivity, or evidence of reflectivity gradient. Some radar data we selected are also more than 10 km seaward of the modern grounding zone. For the basal melt rates (~1 m yr^{-1} from phase-sensitive radar measurements presented by *Marsh et al.* [2016]) and ice speeds in this area, ~20 m of ice has been melted away for ice that is ~10 km from the grounding zone, likely resulting in little or no debris remaining in basal ice. Other factors affecting radar basal reflectivity (e.g., variations in ice temperature and crystal-fabric orientation) likely have minor effects on this calculation (Appendix B).

3.2.4. Basal Reflectivity Uncertainty

The observed basal reflectivity is affected by instrument design, system and target geometry, englacial attenuation rate, and the reflectivity of a target interface [*Matsuoka et al.*, 2010, 2012], which is the quantity of interest. The method of using the long-path multiple to estimate englacial attenuation rate eliminates uncertainty associated with instrumental factors and system geometry [*MacGregor et al.*, 2011]. However, uncertainties associated with target geometry and englacial attenuation of the radar wave remain. We later use waveform modeling to analyze the possible of effect of target geometry on observed reflectivity (see sections 3.4.3, 4.2.2, and 5.2.2). Englacial attenuation depends on ice temperature, chemistry, and crystal-orientation fabric, which are generally poorly known. Ice chemistry throughout the ice column is unlikely to change over our relatively small survey area because the ice is sourced from regions that are likely to have experienced similar weather patterns over the time period preserved in the ice column, and therefore, the ice likely has similar acid and sea salt content. Crystal-orientation fabric likely has negligible effect on reflectivity in this survey due to the comparatively small ice thickness to radar wavelength ratio [*Matsuoka et al.*, 2012]. Assessing the impacts of strain heating on ice temperature requires application of a thermomechanical ice sheet model. Past studies of the effects of a strain heating as ice flows across a grounding zone indicate that englacial attenuation rate (for 5 MHz radar wave) may increase by up to 2 dB/km as ice goes afloat [*Matsuoka et al.*, 2012]. If strain heating were significant in our survey, we would expect to see this decrease in reflectivity along the entire grounding line as the ice goes afloat, and we do not observe this at the subglacial peninsula. In any case, we consider the calculated uncertainty in englacial attenuation rate (2.1 dB km^{-1}) sufficient to account for uncertainty associated with strain heating (Appendix B).

Due to poor knowledge of ice chemistry and temperature and the nonuniqueness of geometric configurations consistent with the radar data, it is generally considered impractical to precisely estimate the uncertainty of basal reflectivity measurements [*Matsuoka et al.*, 2012]. To obtain a rough estimate of the uncertainty in our data, we consider the reflectivity associated with the data used to estimate the englacial attenuation rate, which are reflections from a bright ice-seawater interface (yellow profiles in Figure 2). After correcting for spherical spreading and englacial attenuation, two standard deviations in the observed reflectivity for these profiles is 2.1 dB. We consider this a rough indication of the uncertainty in the basal reflectivity and do not interpret reflectivity changes of less than 2 dB as significant.

3.3. Grounding Line Location

Following *Christianson et al.* [2013], we locate the grounding zone using multiple methods, each of which is sensitive to different attributes. Here we summarize only the most salient points in this approach, some of which have been updated as newer remote-sensing data have become available. First, we used repeat kinematic GPS profiles driven along-flow parallel radar and seismic profiles over one full tidal cycle [*Horgan et al.*, 2013a]. This allows us to place upstream and downstream limits on grounding line location via detection of the upglacier extent of vertical motion at various times in the tidal cycle. Second, the grounding line is always inland of the inland-most extent of seismically imaged water column, which is at least 2 m thick [*Horgan et al.*, 2013a]. Third, where seismic and kinematic data were not collected, we used satellite-based grounding lines derived from differential interferometric synthetic aperture radar (DInSAR) and laser altimetry [*Rignot et al.*, 2011; *Depoorter et al.*, 2014]. Fourth, we used estimates of hydrostatic equilibrium derived from our kinematic GPS data and radar-determined ice thickness with a firn correction [*Christianson et al.*, 2013]; the absolute value is slightly uncertain owing to grounding line motion with the tides, but the upglacier limit of the grounding line at high tide is probably between the 0 and 10 kPa hydropotential contours shown in Figure 2a. Finally, we used characteristic ice-penetrating radar echoes (see later section 6.2) to identify the grounding or subglacial "estuarine zone" [*Horgan et al.*, 2013b]. As the limit of inland tidal flexing is not detected by DInSAR [*Rignot et al.*, 2011] and grounding zone processes may persist inland of the detectable grounding line (the inner limit of tidal motion) [*Walker et al.*, 2013; *Christianson et al.*, 2013; *Horgan et al.*, 2013b], we use all these metrics when considering the grounding zone location, prioritizing based on the information conveyed and the question being asked.

3.4. Radar Basal Reflectivity Modeling

We use dielectric modeling to evaluate the physical mechanisms that could explain the observed basal reflectivity. The model parameters we choose to examine are motivated by physically plausible basal conditions. Previous studies [e.g., *Peters et al.*, 2005; *Anandakrishnan et al.*, 2007; *MacGregor et al.*, 2011] have considered the composition of the basal reflector (dielectric materials and two- versus three-layer interfaces) and the

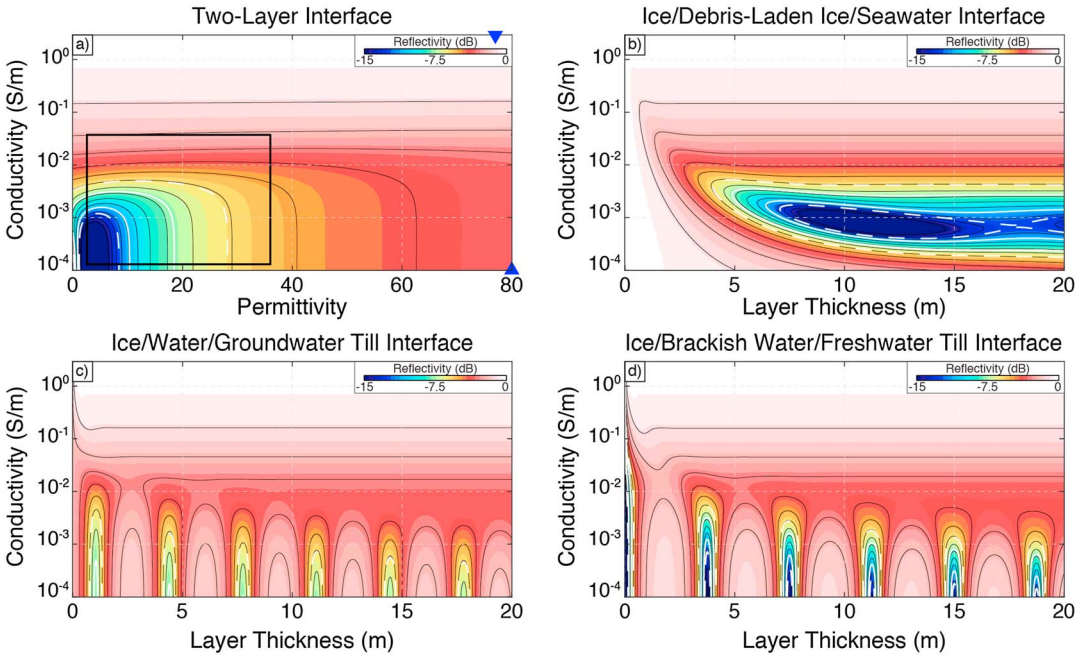

Figure 6. Returned power calculated via amplitude modeling for a 5 MHz radar wave incident on two- and three-layer interfaces. Power returned from (a) a two-layer interface for all likely subglacial materials (see Table 1), (b) an ice debris-laden ice-seawater interface, (c) ice water-groundwater till interface, and (d) ice-brackish water-freshwater till interface. Black lines are 1 dB contours. Thick white lines indicate one (solid) and two standard (dashed) deviations of reflectivity distribution of zone 3 (see text; Figure 11). Dashed box in Figure 6a indicates range of reflectivity returned for all subglacial materials that are not water (see Table 1). Blue triangles indicate reflectivity of an ice-freshwater (low conductivity) and ice-seawater (high conductivity) interface. In Figures 6b–6d, conductivity and middle layer thickness vary. Glacier ice and lower layer dielectric parameters used in Figures 6b–6d are given in the text.

effects of scattering separately. We use full waveform modeling to simultaneously consider the effects of dielectric contrast and scattering on reflectivity. We look first at reflection amplitude and then at waveforms.

3.4.1. Reflection Amplitude Modeling

We model reflection coefficients for several possible basal interface configurations, using both a two-layer and a three-layer model. The power reflection coefficient of a two-layer interface illuminated at normal incidence is given by

$$R_{ab} = 20 \log_{10} \left| \frac{\sqrt{\epsilon_a} - \sqrt{\epsilon_b}}{\sqrt{\epsilon_a} + \sqrt{\epsilon_b}} \right|, \tag{1}$$

where ϵ_a and ϵ_b are the (complex) dielectric coefficients of the upper and lower layer, respectively. However, as the thickness of the ocean (or brackish) water column is on the order of one-fourth radar wavelength (~11.3 m in water for this system) in much of the embayment [*Horgan et al.*, 2013a, 2013b], we must also consider thin-film effects. To do so, we also alternatively model the power reflectivity of the basal reflection using a three-layer model that accounts for multiple reflections and attenuation within the middle layer [*Born and Wolf*, 1999; *MacGregor et al.*, 2011]:

$$R_{abc} = 20 \log_{10} \left| r_{ab} + t_{ab} r_{bc} t_{ab} \frac{\exp\left(-2ik_b\delta\right)}{1 - r_{bc} r_{ab} \exp\left(-2ik_b\delta\right)} \right|, \tag{2}$$

where r and t are the (amplitude) reflection and transmission coefficients (subscripts indicate layer of travel and layer of incidence), k_b is the electromagnetic propagation constant of the middle layer, and δ is the thickness of the middle layer. This model allows destructive interference nodes for low-conductivity materials.

To assess possible compositions of the subglacial interface, we input the permittivities and conductivities of a variety of possible subglacial materials as the lower layers in these two models and always assume the

Table 2. Dielectric Parameters of Medium Modeled Using Fourier Synthesis Shown in Figure 7[a]

Interface	Permittivity Film	Conductivity Film (S m^{-1})	Permittivity Lower Layer	Conductivity Lower Layer (S m^{-1})
Ice-seawater	N/A	N/A	77	2.9
Ice-groundwater till	N/A	N/A	36	0.037
Ice-frozen groundwater till	N/A	N/A	2.9	3.5×10^{-4}
Ice-seawater-groundwater till	77	2.9	36	0.037
Ice-freshwater-groundwater till	80	1.0×10^{-4}	36	0.037
Ice-freshwater-seawater	80	1.0×10^{-4}	77	2.9
Ice-brackish water #1-freshwater till	64	1.0×10^{-4}	6.0	2.0×10^{-4}
Ice-brackish water #2-freshwater till	64	3.0×10^{-3}	6.0	2.0×10^{-4}
Ice debris-laden ice-seawater	3.1	8.0×10^{-5}	77	2.9

[a]In all cases, the upper layer is ice (permittivity is 3.2; conductivity is 7.0×10^{-5} S m^{-1}) that is 750 m thick. The intermediate layer (thin film), if present, is 15 m thick. The lower layer is treated is an infinite half-space.

uppermost layer is glacier ice (Table 1 and Figure 6). We focus on the following four specific scenarios to capture the variable basal interface compositions likely to occur at an ice stream grounding zone:

1. *Two-layer model*. We modeled the power reflection coefficient for glacier ice over all likely subglacial materials (permittivity (ϵ') ranging from 0 to 80; conductivity (σ) ranging from 1×10^{-4} to 2.9 S m^{-1}).
2. *Ice debris-laden ice-seawater interface*. In this scenario, the top layer is glacier ice ($\epsilon' = 3.2; \sigma = 7{\times}10^{-5}$ S m^{-1}), the middle layer is debris-laden ice ($\epsilon' = 3.1$ assuming a 15% debris content (see Table 1); variable till conductivity ranges from $\sigma = 1{\times}10^{-4}$ to 2.9 S m^{-1}; debris-laden ice thickness varies 0 to 20 m), and the bottom layer is seawater ($\epsilon' = 77; \sigma = 2.9$ S m^{-1}).
3. *Ice-water-till interface*. In this scenario, the top layer is glacier ice, the middle layer is variable conductivity water ($\epsilon' = 80$; variable conductivity ranging from $\sigma = 1 \times 10^{-4}$ to 2.9 S m^{-1}; variable water column from 0 to 20 m), and the bottom layer is till of a relatively high conductivity ($\epsilon' = 36; \sigma = 0.037$ S m^{-1}).
4. *Ice-brackish, sediment-rich water-till interface*. In this scenario, the top layer is glacier ice, the middle layer is water with approximately 8% sediment content ($\epsilon' = 64$; variable conductivity ranges from $\sigma = 1 \times 10^{-4}$ to 2.9 S m^{-1}; variable depth from 0 to 20 m), and the bottom layer is till of a relatively low conductivity ($\epsilon' = 6$; $\sigma = 2.0 \times 10^{-4}$ S m^{-1}).

3.4.2. Fourier Waveform Synthesis

To further explore the composition of the basal substrate, we compare the form of the observed basal wavelet to that of theoretical wavelets returned from the basal interfaces listed in Table 2, by using Fourier synthesis [*Arcone et al.*, 2006] to construct a synthetic basal echo for each case (Figure 7 and Table 2). We model the reflected waveform $E_r(t)$ as a triple summation, such that

$$E_r(t) = \sum_i E_i(\omega_i) \sum_p R_p \sum_{mp} T_{mp} \exp(-2ik_i d_{mp} n_{mp}), \tag{3}$$

where $E_i(\omega_i)$ represents the transmitted waveform, R_p is the Fresnel electric field reflection coefficient of each of p successive interfaces, and the final summation accounts for the two-way electric field transmission coefficients between successive interfaces (m above and p below; T_{mp}) where $k = \omega/c$ is the free-space propagation wave number, d_{mp} is the layer thickness, and n_{mp} is the refractive index of the individual layer. The exponential function accounts for the two-way phase delay within individual layers of the medium. Here, as we do not know the precise form of our transmitted wave, we simply used a 5 MHz sinusoid wavelet (+/- phase) sampled at 5 ns (Figure 7a). Both transmitted and reflected waveforms were synthesized using 1000 frequencies covering a bandwidth of 0.25 MHz to 25 MHz in steps of 0.25 MHz. Amplitudes of reflected waveforms are scaled to account for spreading and attenuation within the upper glacier ice layer, but not within lower layers, so that relative amplitudes after the initial reflection are preserved. Dielectric parameters used are shown in Table 2.

3.4.3. Finite-Difference Time Domain Modeling

Our modeling so far has followed most prior work in radioglaciology by considering laterally extensive layers with smooth, specular interfaces or distinct features such as crevasses. We also wish to consider the effects of scattering from a surface with subresolution spatially variable roughness, possibly generated from reflections

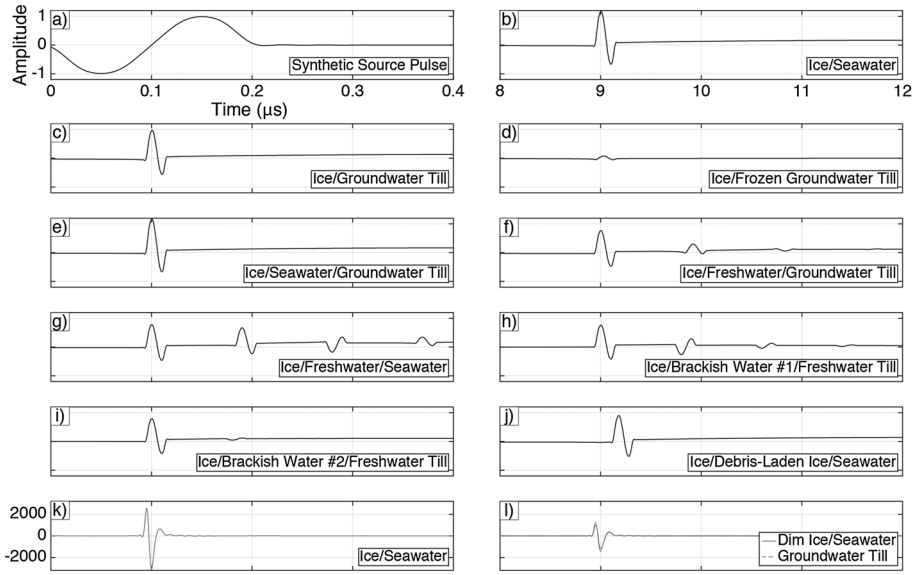

Figure 7. Synthetic waveforms (black) constructed via Fourier synthesis for (a) source pulse at 5 MHz, (b) ice-seawater interface, (c) ice-groundwater till interface, (d) ice-frozen groundwater till interface, (e) ice-seawater-groundwater till interface, (f) ice-freshwater-groundwater till interface, (g) ice-freshwater-seawater interface, (h) ice-brackish water #1-freshwater till interface, (i) ice-brackish water #2-freshwater till interface, and (j) ice debris-laden ice-seawater interface. Observed waveforms (gray) from (k) an ice-seawater interface and (l) dim ice-seawater (solid line) and groundwater till (dashed line) interface. Layer parameters used to construct waveforms are given in Table 2. Reflection amplitude of synthetic waveforms is scaled to account for attenuation of a normal incidence radar wave traversing glacier ice 750 m thick with a relative permittivity of 3.2 and high-frequency conductivity of $7 \cdot 10^{-5}$ S m^{-1}. When not labeled, axes are the same as in the previous plot.

off features such as melt-induced flutes or grooves in the basal interface. A similar approach has been used before to analyze the appearance of moulins in the Greenland ice sheet [*Catania et al.*, 2008].

To assess the possible effect of deviations from basal reflector specularity on our data, we performed two-dimensional finite-difference time domain (FDTD) modeling of radar wave propagation. Using the implementation of *Irving and Knight* [2006], we modeled six geometries (Figure 8):

1. *A smooth ice-seawater interface*. The top layer is glacier ice ($\epsilon' = 3.2$; $\sigma = 7 \times 10^{-5}$ S m^{-1}) and the bottom layer is seawater ($\epsilon' = 77$; $\sigma = 2.9$ S m^{-1}).
2. *An ice-brackish water-groundwater till interface*. The top layer is glacier ice, the middle layer (15 m thick) is brackish water ($\epsilon' = 64$; $\sigma = 1.0 \times 10^{-4}$ S m^{-1}), and the bottom layer is freshwater till ($\epsilon' = 18$; $\sigma = 2.0 \times 10^{-4}$ S m^{-1}).
3. *A sinusoidal ice-seawater interface with amplitude and wavelength below the imaging resolution of this radar system (wavelength 20 m; amplitude 5.75 m; root-mean-square (RMS) height 4 m)*. The top layer is glacier ice and the bottom layer is seawater.
4. *A crevassed ice-seawater interface: crevasses (10 m wide, 10 m high) are inserted into the basal ice at positions, so that the resulting RMS height is 4 m (crevasse superposition is permitted)*. The top layer is glacier ice and the bottom layer is seawater.
5. *An ice debris-laden ice-seawater interface*. The top layer is glacier ice, the middle layer (15 m thick) is debris-laden ice ($\epsilon' = 3.1$; $\sigma = 8.0 \times 10^{-5}$ S m^{-1}), and the bottom layer is seawater.
6. *A sinusoidal ice debris-laden ice-seawater interface with amplitude and wavelength below the imaging resolution of this radar system (wavelength 20 m; amplitude 5.75 m; RMS height 4 m)*. The top layer is glacier ice, the middle layer (15 m thick) is debris-laden ice, and the bottom layer is seawater.

In all FDTD scenarios, the model domain is 1 km wide and 1000 m deep. Array size varies in order to allow maximum possible spatial field discretization without numerical dispersion [*Irving and Knight*, 2006]. The source is a Blackman-Harris pulse with a dominant frequency of 5 MHz (roughly a sine wave with +/- phase). A synthetic trace was acquired every 33 m.

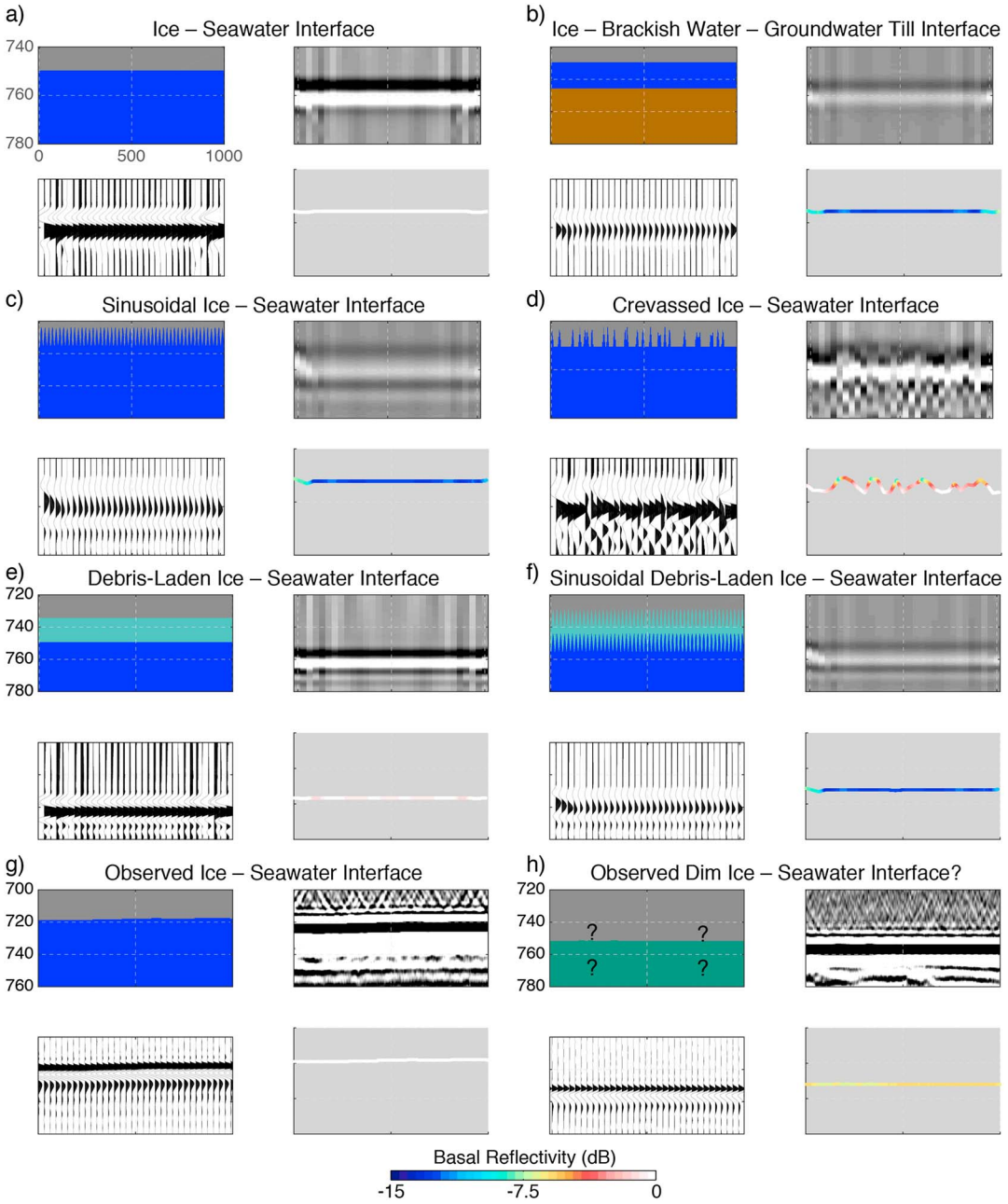

Figure 8. Finite-difference time domain synthetic modeling for six scenarios: (a) an ice-seawater interface, (b) an ice-brackish water-groundwater till interface, (c) an ice-seawater interface with low-amplitude sinusoidal ice-bottom topography below the radar's imaging resolution (RMS height of 4 m), (d) an ice-seawater interface with randomly placed crevasses, (e) an ice debris-laden ice-seawater interface, and (f) an ice debris-laden ice-seawater interface with low-amplitude sinusoidal ice-bottom topography below the radar's imaging resolution (RMS height of 4 m). Observed reflections for (g) an ice-seawater interface and (h) the dim area (zone 4) in the subglacial embayment. For situation, the true geometry (ice in gray, till in brown, debris-laden ice in aqua, and water in blue) is shown in the upper left, the radargram in the upper right, the variable area amplitude plot of the basal return in the lower left, and the basal reflectivity in the lower right. Dielectric parameters of the ice, water, and till input to the model are given in the text. Power reflectivity is calculated assuming a known ice-seawater reflectivity. When not labeled, axes are the same as in the previous plot.

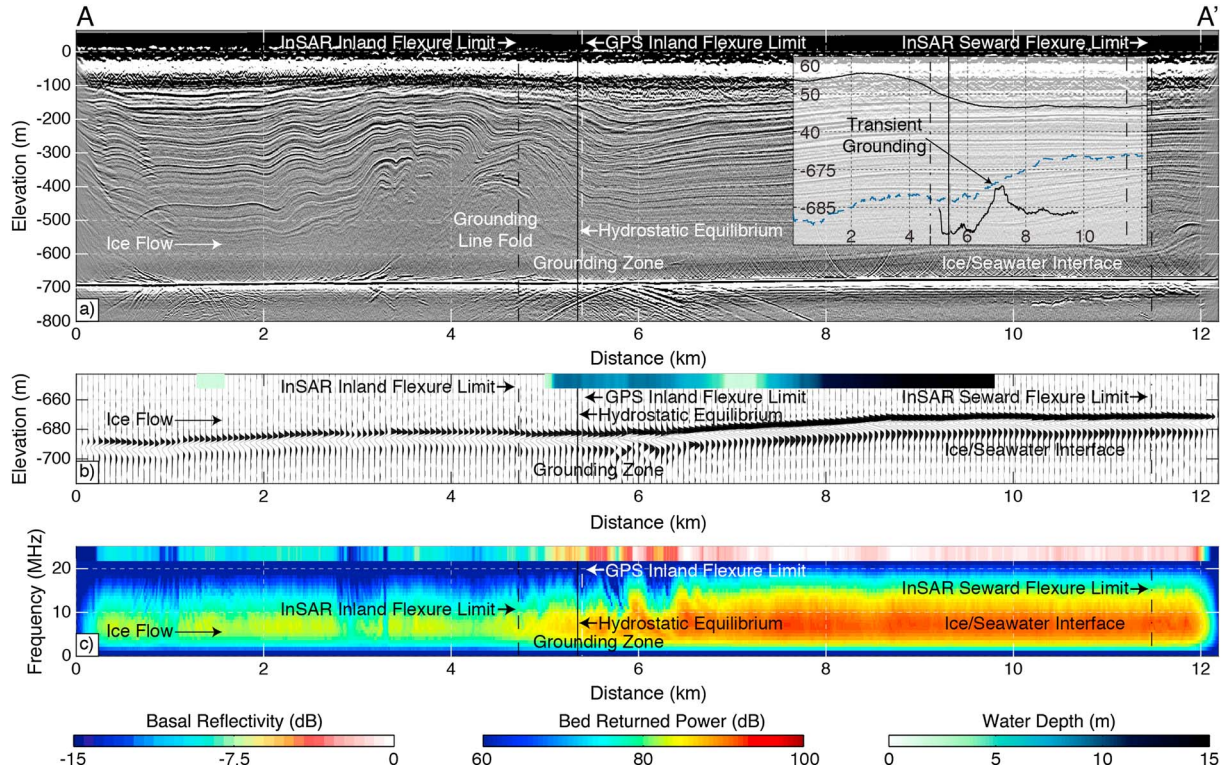

Figure 9. (a) Radar profile AA′ at the Whillans grounding zone (see Figure 2b for profile location), (b) variable area amplitude wiggle plot of basal reflection wavelet, and (c) frequency composition of the basal reflection wavelet. The inset in Figure 9a shows ice sheet geometry and bathymetry. The colorbars in Figures 9b and 9c show ocean water column depth [*Horgan et al.*, 2013a, 2013b] and basal reflectivity, respectively. Grounding lines are from *Rignot et al.* [2011] and *Depoorter et al.* [2014]. Other annotated features are discussed in the text.

4. Results

4.1. Absolute Basal Reflectivity

The basal reflectivity in our survey can be divided into four characteristic zones (Figure 4): (zone 1) inland areas where reflectivity is generally consistent with that of an ice-unfrozen till interface; (zone 2) areas of bright reflectivity in the vicinity of grounding; (zone 3) unambiguously floating areas, as indicated by active-source seismic data [*Horgan et al.*, 2013a, 2013b], where the reflectivity is anomalously low; and (zone 4) floating areas where the basal reflectivity is typical of the high values expected from a specular ice-seawater interface.

In areas well inland of the grounding zone (zone 1), the reflectivity is variable but is generally within the range of −16 to −2 dB.

Zone 2 extends from ~100 to 2000 m inland of the inland limit of the seismically imaged water column and GPS inland flexure limit (Figure 4) and exhibits reflectivity of approximately −4 to −6 dB. We note an artifact in the limited area near the upstream end of the seismically imaged channel in the embayment, where reflectivity is anomalously low because our automated digitizer selected only the upper branch of the bifurcated basal echo (see section 6.3). The finite width of the amplitude detection window therefore results in less energy being captured. As this reflectivity reduction is associated with a basal geometric feature and not solely a change in basal interface dielectric properties, we consider it an anomalous feature within zone 2 rather than a separate reflectivity zone.

Zone 3 occurs just downglacier of the grounding line in the embayment (km 10 to 25 in Figure 10, zone 3 in Figure 4; within ~10 km of the grounding line), where the basal reflectivity is anomalously low (−7 to −11 dB; Figure 11) compared to the expected reflectivity from an ice-seawater interface.

The fourth zone of basal reflectivity has uniformly high amplitude and is located downstream of the grounding zone (Figure 4). The distance from the grounding zone to the onset of this high-reflectivity zone varies greatly. For example, over the subglacial peninsula (line AA′ in Figure 9), the reflectivity transitions from −10 to ~0 dB in a few hundred meters straddling the upstream limit of the seismically detectable seawater.

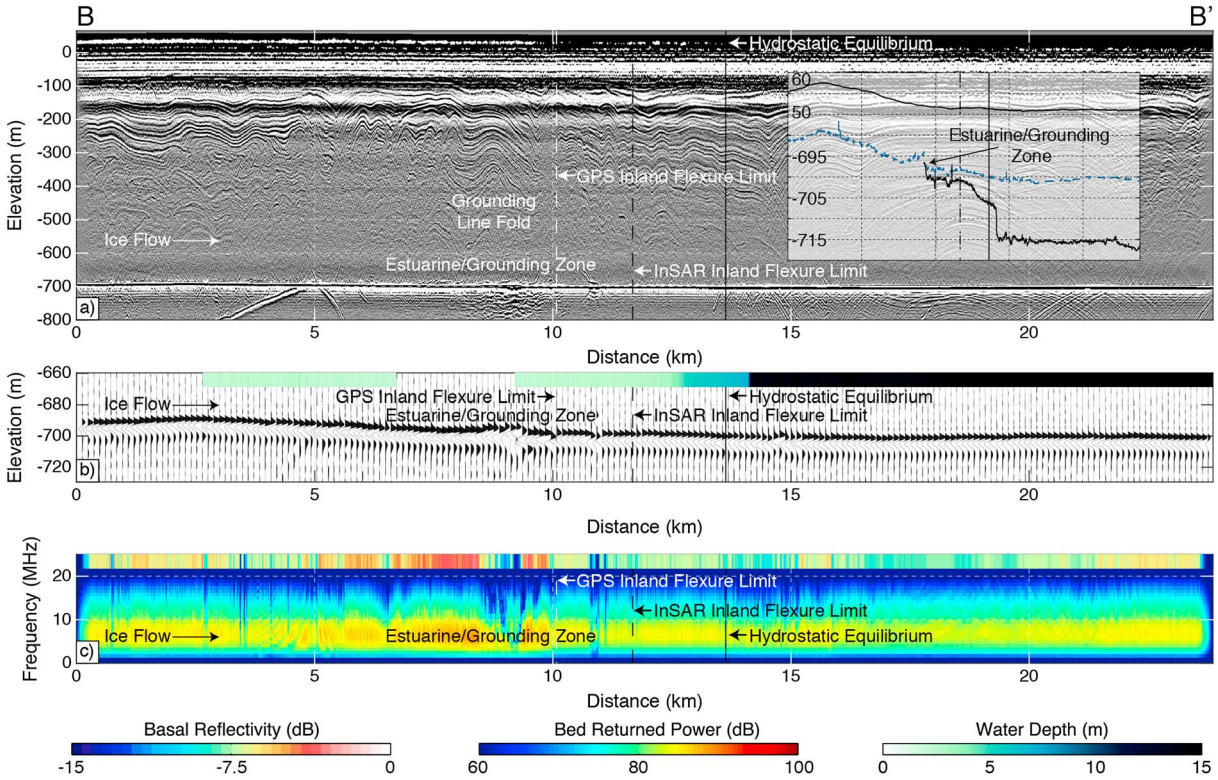

Figure 10. (a) Radar profile BB′ at the Whillans grounding zone (see Figure 2b for profile location), (b) variable area amplitude wiggle plot of basal reflection wavelet, and (c) frequency composition of the basal reflection wavelet. The inset in Figure 10a shows local ice sheet geometry and bathymetry [*Horgan et al.*, 2013a, 2013b]. The colorbars in Figures 10b and 10c show ocean water column depth [*Horgan et al.*, 2013a, 2013b] and basal reflectivity, respectively. Grounding lines are from *Rignot et al.* [2011] and *Depoorter et al.* [2014]. Other annotated features are discussed in the text.

Along this profile, the form of the basal echo is complex in the grounding zone (Figures 9 and 12a) but is relatively simple elsewhere. Within the embayment, no reflectivity similar to zone 4 is observed, though basal reflectivity does eventually transition to zone 4 downstream of the embayment (>10 km seaward from the grounding line).

4.2. Basal Reflectivity Modeling

Comparison between our observations (Figure 4) and our basal reflectivity modeling (Figure 6 and section 3.4) shows that all zones, except for zone 3, are well matched using a specular two-layer model, with different materials in the different zones. Reflectivity zones 1, 2, and 4 correspond to expected reflectivity from a two-layer interface composed of ice and till (of varying conductivity; zones 1 and 2) or ice and seawater (zone 4). The analysis suggests that reflectivity in zone 3 is reduced due to either the presence of a three-layer basal interface causing destructive interference or scattering from a rough interface.

4.2.1. Fourier Waveform Synthesis

Synthetic reflections from a two-layer interface (Figure 7) consist of a single return, similar to that observed outside the grounding zone (Figures 9 and 10). The amplitude of the return varies according to the dielectric contrast across the modeled interface, and the phase is reversed for reflections from water and from thawed till containing groundwater but is not reversed for a reflection from till containing frozen groundwater (see Tables 1 and 2). The reflection from a three-layer interface with a middle layer of seawater is essentially the same as that from an ice-seawater interface due to the high conductivity and thus low skin depth of seawater (~10 cm for a radar wave at 5 MHz; Figure 7e and Table 1). Reflections from other three-layer interfaces include multiple reflections off the interfaces at the top and bottom of the intermediate layer (Figures 7f–7h). The amplitude of echoes that originate from repeated reflections within the intermediate layer are attenuated to varying degrees depending on the conductivity of the intermediate layer, so that for some media only an initial reflection from the top and bottom of the intermediate layer is observed (Figure 7i). The phase of these reflections follows expected patterns, always reversing if the dielectric constant increases as the wave traverses

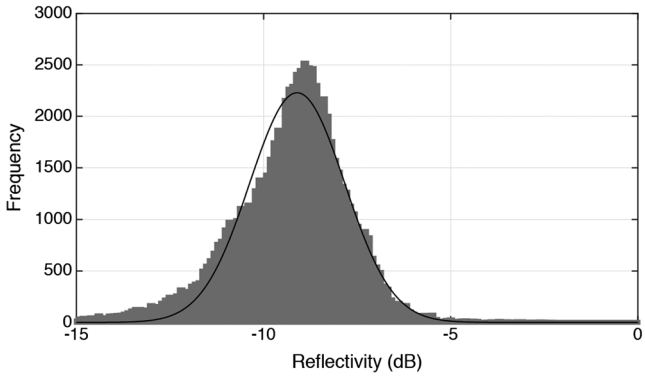

Figure 11. Basal reflectivity distribution within the zone of anomalously low basal reflectivity zone 3 (area between thick black line and grounding line) in Figure 4. Black curve is a Gaussian fit to these data given by a mean and standard deviation of −9.3 dB and 1.6 dB, respectively.

the interface. As noted earlier, with the exception of the long-path multiple, we generally do not observe a spatially consistent reflection arriving later in time than the basal reflection (Figures 9 and 10; section 3.2.3).

In Figures 7k and 7l, we plot observed waveforms from an ice-seawater interface (zone 4), groundwater till interface (zone 1), and anomalously dim ice-seawater interface (zone 3). The waveforms from the groundwater till interface and dim ice-seawater interface are practically indistinguishable. The observed dim reflection from an "unknown" interface (zone 3) is most similar to the modeled reflection from either an ice/brackish water/freshwater till interface (Figure 7k) or ice/debris-laden ice/seawater interface (Figure 7l).

4.2.2. Finite-Difference Time Domain Modeling

Figure 8 shows results from the FDTD modeling. In all cases, the phase of the basal wavelet is reversed, as expected, and the amplitude of the return is reduced in the cases where scattering occurs. The ice-brackish water-till interface and sinusoid bed interface have essentially the same radar return with the sinusoid bed showing a slightly wider (in travel time) bed echo (Figures 8b and 8c). These returns are qualitatively similar to returns from a sinusoidal debris-laden ice-seawater interface (Figure 8f). In these simulations, the conductivity of the debris-laden ice is quite low ($\sigma = 8.0 \times 10^{-5}$ S m^{-1}), and thus, the dielectric properties of the debris-laden ice are similar to those of clean ice. Hence, the return from the debris-laden ice-seawater interface (Figure 8e) is only slightly dimmer than that from the ice-seawater interface (Figure 8a) due to the slightly lower dielectric permittivity of the debris-laden ice. Most of the reduction in amplitude of the return from the sinusoidal debris-laden ice-seawater interface (Figure 8f) is due to the roughness of the ice bottom.

We plot the observed returns from an ice-seawater interface and anomalously dim ice-seawater interface in Figures 8g and 8h, respectively. The decrease in reflectivity due to a rough basal interface is more than sufficient to account for the observed dim interface in zone 3.

5. Interpretation

5.1. Absolute Basal Reflectivity

Values of absolute basal reflectivity well inland of the grounding zone are those expected for an ice-unfrozen till or ice-unfrozen bedrock interface (−16 to −2 dB; Table 1; Zone 1 in Figure 4). We do not image reflectivity typical of an ice-frozen bedrock interface in our survey. The variability of the reflectivity in this zone is likely due to spatially heterogeneous subglacial hydrological and sedimentological conditions (examples of different compositions of till-water interfaces and their reflectivities are given in Table 1), but generally, the reflectivity is as expected for an ice-till interface (−7 to −10 dB for a till layer at least several meters thick; Figure 6 and Table 1), with occasional lower reflectivity indicative of less water in the till matrix. Although there may also be significant sediment (up to ~10 to 20%) entrained into the basal ice [*Engelhardt and Kamb*, 2013], the lack of strong dielectric contrast between ice and entrained rock (Table 1; here modeled as a mixture of sand and ice) and the likely gradual changes in sediment concentration at the top of the debris-laden basal ice layer [*Bender et al.*, 2011] make detection and identification of an unambiguous ice-sediment-rich ice or ice-sediment-rich ice-till interface difficult. Our inference of a relatively thick (several meters or more) subglacial till layer is corroborated by reflection seismology [*Horgan et al.*, 2013a]. Because there is no indication of a spatially continuous, subbasal reflection, and the bed wavelet form indicates a single interface (i.e., not a superposition of multiple reflections from nearby layers; Figures 9 and 10), it is unlikely that this radar can

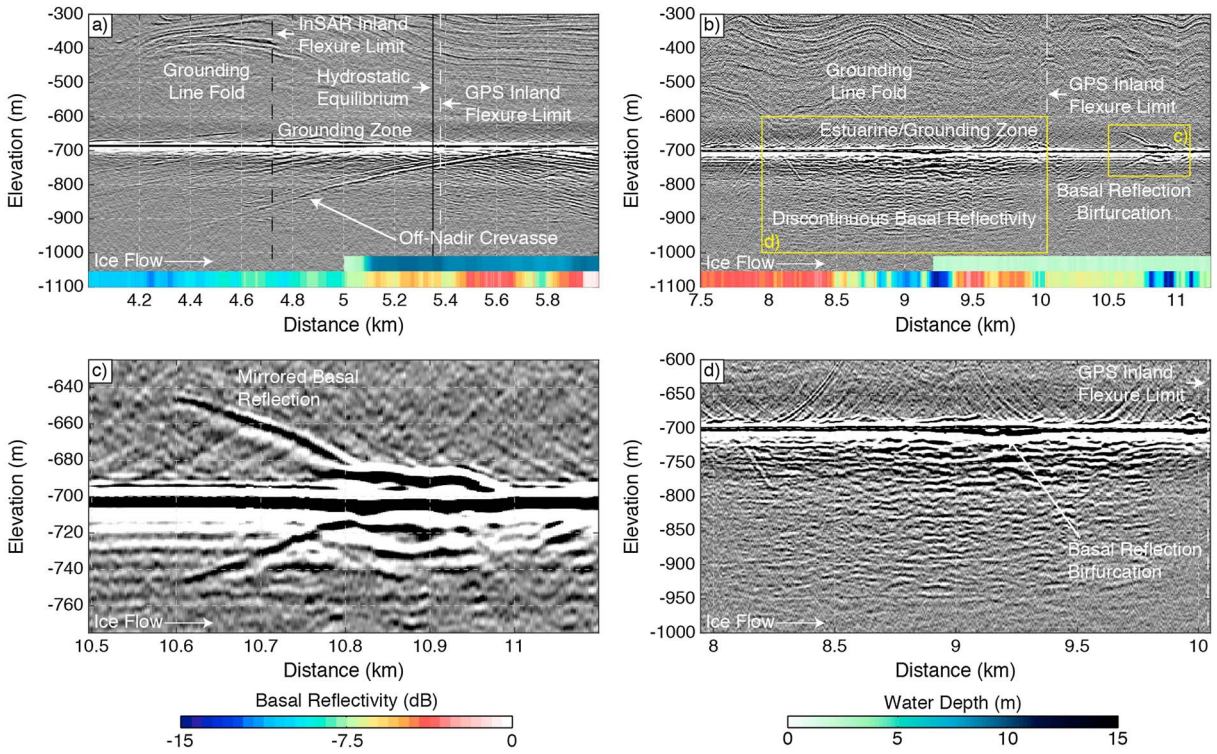

Figure 12. Expansions of specific features in radar data: (a) grounding zone on line AA′, (b) grounding zone on line BB′, (c) enlargement of reflection from subglacial crevasse(s) shown in yellow box in Figure 12b, and (d) enlargement of subglacial sediment deposit or channel shown in yellow box in Figure 12b. Colorbars indicate basal reflectivity and subglacial water column depth. Annotated features are discussed in the text.

image through the thick (~10 to 19 m) till layer [*Horgan et al.*, 2013a]. Indeed, in order for this to occur, the till conductivity would have to be abnormally low ($<10^{-4}$ S m^{-1}), which would only be associated with especially pure water and low-conductivity sediments.

Reflectivity in zone 2 is consistent with an ice-till contact (Figures 6 and 10 and Table 1). Most likely, the basal interface is an "ice-groundwater till" interface, where water in the till matrix is more conductive than farther upstream due to tidal flexure effects, which may pump seawater through the till matrix inland of the grounding line [*Walker et al.*, 2013], increasing the bulk conductivity of the till. Our results show enhanced bright reflectivity up to 2 km inland of the seismically imaged grounding line (Figures 10 and 12a), which indicates that some seawater infiltration inland of grounding may be possible. This is consistent with tidally driven water flow exceeding the hydropotential gradient immediately upstream of grounding and the estuarine nature of this embayment [*Horgan et al.*, 2013b].

Reflectivity is anomalously low in zone 3 despite the presence of a substantial subglacial water column (generally ~14 to 16 m thick; Figures 2 and 13), as indicated by reflection seismology [*Horgan et al.*, 2013a, 2013b] and several remotely sensed and in situ grounding line metrics [*Horgan and Anandakrishnan*, 2006; *Brunt et al.*, 2010; *Rignot et al.*, 2011; *Christianson et al.*, 2013; *Depoorter et al.*, 2014]. Nowhere in zone 3 do we image a spatially continuous first multiple of the basal reflection as we do farther afloat (Figures 5, 9, and 10). From interpretation of basal reflectivity alone, rough, debris-laden ice that scatters radar wave energy or thin-film destructive interference effects arising from an ice-water-till interface are equally likely explanations for the low radar reflectivity. In section 5.2, we use dielectric amplitude and waveform modeling to further explore these possibilities.

Zone 4 is indicative of an ice-seawater interface. The transition in reflectivity over the subglacial peninsula (line AA′ in Figure 9; Figure 12b) is as expected over an ice sheet grounding zone (Table 1). The complex waveform observed in the grounding zone likely results from echoes off of subglacial crevasses. In most of our profiles on the floating ice of the embayment the reflectivity eventually brightens downstream to that consistent with an ice-seawater interface (Figure 4).

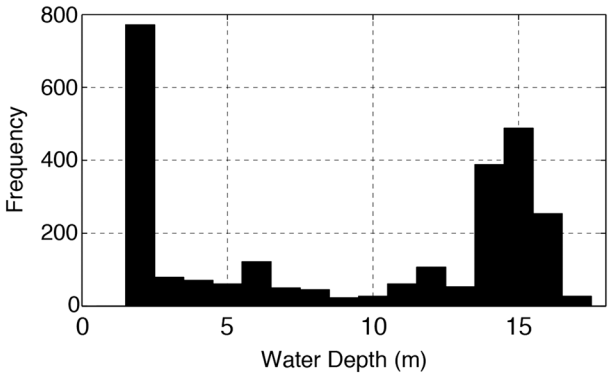

Figure 13. Water depth distribution within the subglacial embayment from active-source seismic data [*Horgan et al.*, 2013a, 2013b].

5.2. Basal Reflectivity Modeling

As explained above (see sections 4.1 and 5.1), the reflectivity in zones 1, 2, and 4 can be explained by a two-layer interface in a straightforward manner. Interpretation of the reflectivity in zones 1 and 4 is straightforward (see section 5.1). Interpretation of reflectivity from zone 2 is complicated by grounding zone effects (see section 4.1), but the reflection still clearly originates from a two-layer interface. Here we use our modeling experiments to explain the more complex basal reflectivity in zone 3, which is inconsistent with the reflection from a simple ice-seawater interface.

The dim reflectivity in zone 3 (Figure 11) and seismic evidence of ice over a roughly 15 m thick water column (Figure 13) are inconsistent with any of our specular two-layer reflectivity models for ice and water. The ice-brackish water-till combination has destructive interference node placement and width consistent with the observed reflectivity in zone 3, suggesting the possibility that the basal interface in this zone may be of this composition (Figures 11–13 and 6d). However, the reflectivity in this zone is also consistent with an ice debris-laden ice-seawater interface (Figure 6b) for debris-laden ice of certain conductivities and thickness. As there are difficulties with the water thin-film model (see section 5.2.1), an ice debris-laden ice-seawater model may be preferable, with basal roughness also likely affecting reflectivity (see section 4.2.2).

5.2.1. Fourier Waveform Synthesis

Overall, these Fourier synthesis analyses are consistent with our earlier amplitude analysis (section 5.1), indicating grounded ice over variable but thawed till (zones 1 and 2 in Figure 4) and ice over seawater in the peninsula area and well downstream in the embayment (zone 4 in Figure 4).

Zone 3 (Figure 4), with weak reflections from floating ice near the grounding zone in the embayment, remains enigmatic. Based on this Fourier synthesis modeling, the most likely configuration is either ice over debris-laden ice over seawater, or ice overlying brackish and probably sediment-laden water overlying a thawed till containing relatively fresh water in the pores, not unlike the suggested interface configuration from the amplitude analysis (section 5.1). However, our understanding of the physical setting [*Jenkins and Doake*, 1991; *Holland and Jenkins*, 1999; *Jenkins*, 2011] suggests that tidal mixing associated with the observed tidal rise and fall of the ice in this region would yield more nearly normal marine salinities, as freshwater fluxes from beneath the grounded ice [*Fricker and Scambos*, 2009; *Christianson et al.*, 2012] and from basal melting [*Marsh et al.*, 2016] are small compared to tidal flows. Furthermore, recent direct conductivity, depth, and temperature (CTD) observations from subglacial access drilling at the grounding zone do not indicate extensive brackish water (J. Mikucki, personal communication, 2015). Instead, a more likely answer to this puzzle may be that the reduced reflections arise from roughness and from scattering off discrete inclusions, as discussed next.

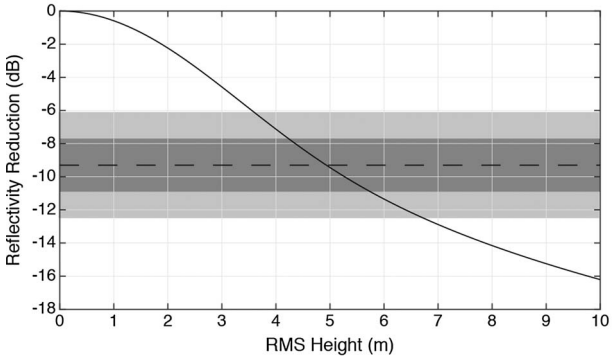

Figure 14. Modeled reflectivity reduction as a function of reflector RMS height following equation (D1). Dashed black line and gray shadings indicate mean, one (dark gray) and two (light gray) standard deviations, respectively, of the anomalously dim reflectivity in zone 3 in Figure 4.

5.2.2. Finite-Difference Time Domain Modeling

Conceptually, roughness smaller than the imaging resolution of the system lowers reflection amplitude compared to a smooth

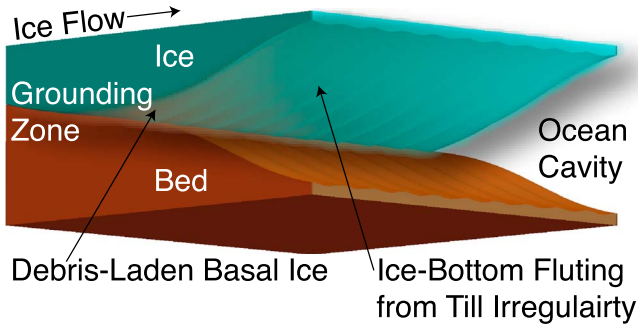

Figure 15. Conceptual model of ice-bottom fluting. Fluting is generated in the basal ice by lobate or ridged sedimentation in the grounding zone that channelizes the water flow and localizes melting. A layer of debris-laden basal ice (up to ~15 m thick) is likely also present. As ice goes afloat and flows into the embayment, the lack of strong thermohaline circulation and the gradually decreasing influence of the deeper bed on water flow allow the fluting to melt off and debris to melt out, leading to a flatter and more nearly specular reflector. For simplicity, this schematic illustrates fluting at only a single wavelength; however, our data suggest that fluting develops at multiple, superimposed wavelengths.

interface by scattering energy away from the nadir direction [*Ulaby et al.*, 1982; *Ogilvy*, 1991; *Shepard et al.*, 2001; *Peters et al.*, 2005; *MacGregor et al.*, 2013]. For antennas that receive energy from nadir, this effect can be quantified using simple expressions derived from Kirchhoff theory [*Peters et al.*, 2005; *MacGregor et al.*, 2013] (Appendix C). Our analysis (Figure 14 and Appendix C) indicates that for our system, basal roughness below the radar's imaging resolution (here the imaging resolution is $\lambda_{ice}/4 = 8.5$ m for a 5 MHz radar wave) could reduce basal reflectivity by nearly 15 dB. Thus, the dim reflectivity of the basal reflector we observe in the embayment could result partially or completely from a basal interface with a root-mean-square (RMS) height of ~4 m (Figure 14). FDTD modeling allows us to quantitatively match the form of the basal wavelet to various basal interface compositions that include a consideration of roughness.

The inference that there is no extensive brackish water layer in zone 3 implicates roughness as the most likely reason for the reduction in basal reflectivity. Our FDTD modeling reinforces this conclusion. The basal reflectivity observed in zone 3 best matches the rough bed with debris-rich basal layer modeling scenario shown in Figure 8f. Following earlier studies [*Peters et al.*, 2005; *Anandakrishnan et al.*, 2007], we assume low-conductivity sediment in the debris-laden ice. Higher-conductivity till could result in thin-film interference effects or, for high enough conductivities, lack of radar wave penetration into the debris-laden ice (as shown in Figure 6), but we do not observe reflectivity or reflector waveforms that indicate high-conductivity till in zone 3. We also do not observe the apparent high variability in basal reflectivity, waveform, and ice-bottom topography that would result from reflections from widespread, irregularly spaced, low-amplitude basal crevasses (Figure 8d). The observed basal wavelet in zone 3 actually exhibits minimal spatial variation in form or frequency content (Figures 9 and 10), similar to that produced in modeling scenarios in Figures 8b, 8c, and 8e. Thus, the most likely composition of the basal interface in zone 3 is rough, debris-laden basal ice over seawater.

5.2.3. Physical Nature of the "Dim" Ice-Seawater Interface

Our modeling analyses indicate that of the physically plausible explanations for the anomalously dim bed return in the embayment, the best fit is provided by rough, debris-laden basal ice that overlies seawater, such that the interface scatters incident radar waves rather diffusely (Figure 8f). However, from the radar data alone, we cannot eliminate the possibility of a reflection from an interface that consists of ice over a thin film of brackish, sediment-rich water, as has been suggested to occur elsewhere on the Siple Coast [*MacGregor et al.*, 2011]. Recent subglacial access drilling at the Whillans Ice Stream grounding zone in this embayment eliminates the possibility of extensive brackish water but does reveal debris-rich basal ice with variable, subresolvable ice-bottom topography, and widespread clasts and sediment that are melting out of the ice [*Scherer et al.*, 2015]. There also is evidence of strong tidal mixing, including flux of visible suspended sediment inland and seaward as the tide advances and then retreats. These observations are at odds with a three-layer model of ice-brackish water-till (Figures 6 and 7), indicating that scattering is important, whether from discrete inclusions in the basal ice, a rough ice-bottom topography, or both.

During melt-out of debris from the base of floating ice, scattering from individual clasts will decrease, but clasts falling out of the ice will leave a rough ice-water scattering interface. Borehole observations indicate that individual clasts are sufficiently small relative to the radar wavelength that scattering will not be large from them or from an interface directly roughened by their fall out. However, sediment may be contained in clumps

and have water around clasts, fluting may give variations in rock-sediment-layer thickness, and melting may create local topography as clusters of clasts fall out of the basal ice (Figure 15). Thus, we consider a rough basal interface and diffuse scattering off sediment as it melts out of the basal ice to be the most likely cause of low reflectivity in the embayment, with higher reflectivity farther downstream after the debris has melted out. At the peninsula, higher basal melt rates evident in the ice thickness profile cause this reflectivity transition to occur over a shorter distance closer to the grounding line.

We cannot fully explain why the downglacier increase in reflectivity (from zone 3 into zone 4; Figure 4) in the embayment is so strong and abrupt. One possibility is that this sharp boundary represents a change in basal ice character that formed somewhere upglacier and is being advected through our study area, although this would require an unlikely coincidence. Another possibility is that there has been a recent upglacier shift in grounding line position, perhaps in response to thinning caused by tension from the rapidly moving ice shelf in response the ongoing slowing of the ice stream [e.g., *Winberry et al.*, 2014], such that sediment-rich basal ice has been newly exposed to the ocean.

6. Grounding Zone Features: Observations and Interpretation

Here we describe additional features in the grounding zone radar data that extend the results from reflectivity. These include IRH deformation, discontinuous basal reflectivity, and bifurcated and mirrored basal reflections. We use reflection seismology, laser altimetry, and DInSAR to inform our interpretation. In sections 6.1 – 6.4, we present observations in the first paragraph and interpret these data in the paragraphs that follow.

6.1. Internal Layers Folds

As reported in *Christianson et al.* [2013], we observe folded internal-reflecting horizons just upstream of the grounding zone (Figures 9 and 10) (see Figure 1 in *Christianson et al.* [2013] for fold locations). These folds deform internal layers for the entire imaged ice thickness. Fold wavelengths are 1 – 2 km with maximum amplitudes of up to several hundred meters occurring near the bed and minimum amplitudes at the ice surface, which itself is slightly raised over the folds.

In *Christianson et al.* [2013], we used a higher-order ice flow model to show that these IRH folds (Figures 9 and 10) may be created due to ice flow over an area of anomalously high basal shear stress just upstream of the grounding line. This zone of high basal friction is likely created by repeated tidal flexure over a wavelength of a few ice thicknesses upglacier, compacting and dewatering the till beneath, thereby increasing basal friction [*Walker et al.*, 2013; *Murray and Clarke*, 1995; *Lekarp et al.*, 2000]. Although our observations are specific to this single embayment of Whillans Ice Stream, any grounding zone with sufficient till and tidal flexure may create such a zone of high basal friction. And in places that lack sufficient accommodation space to create high-relief grounding zone sediment wedges that would provide form and dynamic drag, such as this subglacial embayment [*Horgan et al.*, 2013a, 2013b], this compaction process is likely especially important for grounding zone stabilization. Identification of similar folds in IRHs at other ice sheet grounding zones would lead to better understanding of nontopographic grounding line stabilization.

6.2. Discontinuous Basal Reflectivity

In the grounding zone in the embayment, we image a consistent zone of semicontinuous, nonhyperbolic echoes that begin coincident with the basal echo and extend to apparent depths of nearly 300 m "below" the basal reflector (Figures 10, 12b, and 12d). These returns occur over ~1.5 km downstream from near the hydrostatic flotation grounding line, which is ~1 km upstream of the seismically imaged water column (water thickness $\geq$2 m) (Figures 10, 12b, and 12d). Individual echoes are traceable for one to a few hundred meters in the along-flow direction. We note that these features are generally not present in the few profiles collected over the grounding zone at the subglacial peninsula (Figures 9 and 12a).

We hypothesize that the semicontinuous returns arise from similar features, with the "deeper" returns from off-nadir targets imaged on either side of the radar traverse path, thus explaining the greater arrival times. These features likely form near the upglacier limit of flotation (~0 m water depth), although we cannot resolve in detail the precise origin relative to the tidally migrating grounding line. Interpretation is complicated by the tortuous shape of the grounding line, which in some places runs more nearly parallel than perpendicular to ice flow, so that some of our along-flow radar lines are nearly parallel to and not far from the grounding line.

The dielectric contrast between debris-laden and clean ice is not large enough to explain the high returned power of these features (see section 5.2.3 for discussion of basal reflectivity). Instead, the strength of the

returns and the physical setting suggest that these features arise from reflections from flutings in the base of the ice (Figure 15), in contact with water or wet sediment, or possibly from sediment beneath very shallow and quite fresh water. Continuity of the features along flow is of order hundreds of meters, and the transverse wavelength is probably of order of meters; a transverse wavelength too much larger would allow us to resolve them individually, whereas a notably smaller wavelength would cause them to merge into a uniformly weak reflector rather than discrete reflections. Such shorter wavelengths may be present as well, contributing to the dim reflectivity observed in zone 3. The along-flow continuity of these reflections indicates that the echoes originate from features elongated parallel to flow and not from individual boulders or aggregates of clasts melting out of the ice, nor from crevasses, which yield features described below (section 6.4).

We now consider the conditions leading to the origin of the along-flow discontinuous reflectors with the caveat that we have not imaged individual features clearly nor characterized their time evolution, so additional studies would be needed to test our hypotheses. As flotation begins, sedimentation occurs through some combination of melt-out from basal ice and loss of traction on deforming till, perhaps occasionally with additional sedimentation from dissipation of outburst floods. This sedimentation in and just downglacier of the zone influenced by tidal grounding line migration must interact with the strong tidal inflow and outflow of seawater and with compaction of sediment contacting the moving ice during falling tides. We consider it most likely that the sediment produces debris-flow-type lobes (see section 7.1) and that channelization of water flow between these lobes causes preferential melting to generate flutes in the ice above. The radar may penetrate sufficiently shallow and brackish water to image the upper surface of the sediment as well as the base of the ice. We cannot exclude the possibility that the positive relief occurs not over the water channels but over sediment acting something like the longer-wavelength megascale glacial lineations that are so common on deglaciated continental shelves [e.g., *Anderson et al.*, 2002]. However, the features we image disappear upglacier near the onset of fully grounded ice rather than extending under grounded ice, whereas well-developed megascale glacial lineations probably continue beneath grounded ice [*Anderson et al.*, 2002]. In our preferred model, the flutings incised into the base of the ice may be removed by melting farther downglacier where the water is deep enough that the bed topography no longer strongly channelizes the tidal flow (Figure 15), perhaps still in the zone where tidal mixing suppresses the thermohaline circulation [*Jenkins and Doake*, 1991; *Holland and Jenkins*, 1999; *Jenkins*, 2011] so that it cannot maintain and expand channels in the ice.

At the peninsula, where these features are generally absent, basal melting probably is faster based on physical understanding and the observed more rapid along-flow decrease in ice thickness just downglacier of the grounding line. Seismic imaging shows that the resulting rapid deposition of melt-out sediment has formed a small grounding zone sediment bump with a steeper ice-distal face that likely helps control the current grounding line position [*Horgan et al.*, 2013a], consistent with the morphology of other marine grounding zone wedges [e.g., *Dowdeswell and Fugelli*, 2012]. The location of this sediment bump may also be partially controlled by additional positive topography lower in the sediment column [*Horgan et al.*, 2013a]. A similar, but larger sediment deposit is located ~2 km downstream, which has much higher-amplitude positive topography in the sediment column below it; the ice ephemerally grounds here, suggesting the possibility of recent or ongoing grounding line migration. The steeper seafloor slopes at the peninsula may sufficiently limit the along-flow extent of debris-flow lobes channelizing ice-contact tidal flows that localized strong channels are not melted into the ice. The steeper slopes also likely allow vigorous mixing, suppressing brackish waters that could allow radar imaging of the submarine sediment bed, while also rapidly dropping the sediment bed beyond the radar penetration depth even in brackish water.

6.3. Basal Reflector Bifurcation

In some radar profiles in the embayment, we see an apparent bifurcation of the basal echo within the zone of sediment deposition just discussed (e.g., Figures 10, 12b, and 12d). This bifurcation is visible ~100 m upstream and downstream of the inland limit of the seismically imaged water column.

One possible interpretation of this return is a thin basal channel filled with water fresh enough that the lower echo is still detectable (if the channel were filled with seawater, the seawaters high conductivity would preclude seeing the channel bottom). If this interpretation were correct, the phase of the lower return would be reversed relative to the ice-water interface and the channel dimension would need to be more than several meters in thickness, according to our modeling with synthetic waveforms at this frequency

(see section 5.2.1). Given the overlap in time of the two echoes, it is difficult to resolve a phase reversal, if indeed it is present.

A more likely explanation, given the propensity for this radar to give strong returns from off-nadir, is that these double echoes result from short sections of ridge-like structures, such as those discussed in the section 6.2. The brighter echoes result from more continuous, higher-amplitude, or more favorably located features. Again, we cannot exclude the possibility that these are megascale glacial lineations [e.g., *Anderson et al.*, 2002; *Dowdeswell and Fugelli*, 2012], or sediment lobes imaged through brackish waters, or some combination of these, although features melted into the ice seem most likely because these features are found well downstream of the grounding line where the ice is fully afloat. In any case, these features are a signature in our profiles of the region just downglacier of where ice comes afloat.

6.4. Mirrored Basal Reflections

Another feature in the radar record that occurs as part of the signature of the grounding zone in some of our profiles is a mirror-like echo (near km 1 and 3 in Figure 9, km 11 in Figure 10, and Figures 12b and 12c). These peculiar mirrored echo patterns were first discussed in *Jacobel et al.* [2014]. These echoes appear in eight profiles, two along-flow and six across-flow, in an arcuate pattern immediately downstream of the zone of discontinuous basal reflectivity in the embayment [see *Jacobel et al.*, 2014, Figure 1]. Figure 12c is a radargram enlargement showing one of these mirror echoes along profile BB′. In addition to the near symmetry of the echoes at arrival times both longer and shorter than the basal return, the phase of the echo is the same for both branches, which is the same as the basal echo (white-black-white). Notably, the later return is generally about 10 dB weaker than the earlier arrival. Also, the dip angle of the features imaged by these returns is always in the direction of ice flow, so that the double image appears to open toward the direction of flow, with the highest point/apex upglacier of the intersection of the feature with the base of the ice shelf. In contrast to the mirrored echoes associated with the grounding zone we just described, many other basal-mimicking echoes in the data have reversed phase relative to the basal reflection and appear at arrival times later than the nadir. As such, they mimic returns from "below" the bed because that is where they plot in radargrams. They more likely arise from off-nadir returns in which energy reflects from the highly reflective basal interface, either prior or subsequent to reflection from the feature, producing the inverted phase and the later arrival time.

Jacobel et al. [2014] hypothesized that the mirrored basal echoes were returns from parallel crevasses produced in areas of high stress at both margins of a water-filled channel in the basal substrate just where the ice comes afloat. The arcuate pattern of these crevasses was thus interpreted as a trace of the channel and the grounding line. We suggest that the data are more consistent with a long basal crevasse or series of crevasses located just downstream of the grounding line, striking along the grounding line and dipping in the downflow direction. The upper branch of the crevasse echo signature is indicative of the actual dip and strike of the crevasse. The lower branch (later in time) results from a return following two reflections from the basal interface, one before and one after reflection from the crevasse (Figure 16). Thus, energy travels from the transmitter to be reflected from the wet basal interface, then upward to be reflected from the crevasse, then back to be reflected from the bed again, and finally to the receiver. The returned power from the later return is lower due to reflection off the basal interface (reduction of ~6 to 8 dB in this region and additional englacial attenuation as the radar wave travels through the ice after initially intersecting the crevasse. Thus, three reflections account for the correct phase of the echo relative to the upper branch, the 10 dB reduction in power, and the mirror-like geometry of the features seen. We note that given the wide beam pattern of the radar antennas, the reflections need not be perfectly specular in order for energy to be returned to the receiver. This accounts for the slightly "fuzzy" appearance of the lower branch. These crevasses are created as the ice goes afloat and will contribute to formation of rough ice-bottom topography, which then will be gradually smoothed downflow by basal melt in the subice ocean cavity.

Although data are sparse, the consistent observed downglacier dip angle of these mirror-like crevasses is consistent with opening of tensile cracks in a stress state with strong basal drag and has the opposite sense from an initially vertical crevasse rotated by basal shear. These features likely form in the grounding zone during low tide or just upglacier of the grounding zone, followed by transport with the moving ice but without much cumulative deformation.

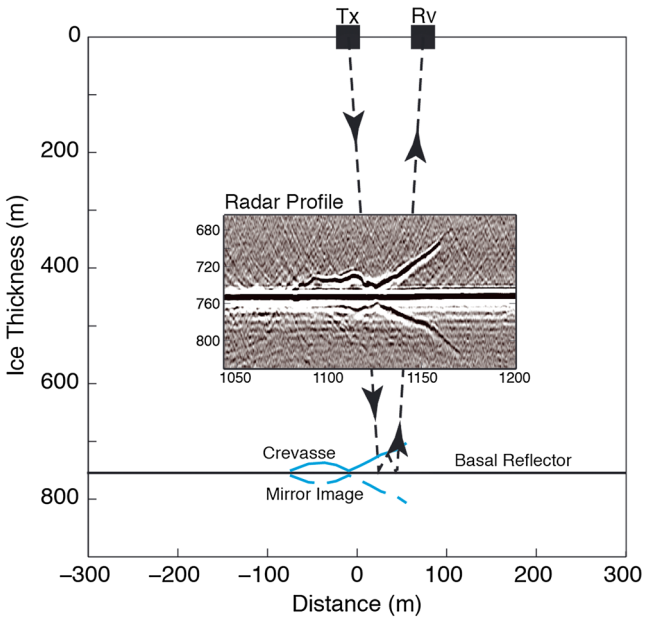

Figure 16. Schematic indicating radar wave raypath that creates mirror-like reflection from basal crevasses. The upper branch of the direct crevasse echo signature is indicative of its true geometry. The lower branch (later in time) results from a return following two reflections from the basal interface, one before and one following reflection from the crevasse.

The colocation of basal crevasses with the grounding line is expected as changes in basal drag are greatest where ice transitions abruptly from contact with the bed to flotation [*Jezek and Bentley*, 1983; *Jezek*, 1984; *Logan et al.*, 2013]. So, in principle, an analysis of the full pattern of crevassing, including other crevasses as well as the mirror-like returns, should reveal extensive information about the state of stress at the bed. But the details of crevasse location, orientation and the patterns of their spatial distribution are challenging to interpret in terms of ice dynamics without more information. The arcuate pattern of the mirror crevasses described above is closely associated with other indications of grounding, but we have found other basal crevasses both upglacier and downglacier of the grounding line, so the full interpretation of the larger pattern of basal stress is not straightforward and is complicated further by the complex shape of the grounding zone, especially in the embayment.

7. Synthesis

In this section, we synthesize our radar observations, modeling results, and interpretations to present a holistic picture of the grounding zone investigated by our radar survey on Whillans Ice Stream. Our conclusions generally start from an interpretation of the observed basal reflectivity then integrate the grounding zone features discussed in section 6 and finally incorporate the results of previous studies. We focus particularly on the nature of the subglacial interface, ice-ocean interactions, and the ramifications of our conclusions for grounding zone stability. Although our conclusions are interpretative, they are based on a consistent integration of our radar observations, modeling, and results of previous studies. Additional field observations are required to confirm our interpretations.

7.1. Basal Interface Composition

Well upstream of the embayment, basal reflectivity is consistent with an interface where grounded ice overlies thawed, water-saturated till. Farther downstream but still upstream of the grounding zone, the basal reflector strengthens, as the radar wave returns from an interface of ice overlying more conductive water, where seawater has possibly been forced upstream of the grounding zone via tidal flexure, especially along the hydropotential low/channel in the embayment and spreading behind the grounding zone ridge associated with tidal flexure. Straddling the seismically detected grounding line, and thus either downglacier of the true grounding line or possibly straddling it (especially in the zone of tidally driven grounding line migration), the basal reflector is weak, with more energy arriving after the basal reflector, likely because the

bed becomes fluted and the flutes scatter energy. Strengthening of subglacial till caused by compression under tidally driven flexure [*Walker et al.*, 2013] may contribute to the origin of this enhanced fluting, and channelization of the tidal water flow by sediment debris-flow lobes or in other ways is likely important. This complex zone is manifested in the radar data as a reduction in basal reflectivity underlying the grounding zone fold in IRH [cf. *Christianson et al.*, 2013], just upstream of the area of inferred basal flute formation. Folding from compression along flow in this grounding zone [*Christianson et al.*, 2013], perhaps also with transverse folding associated with the fluting, may also notably affect the thickness of debris-laden ice. The high temperature of the deepest ice likely means that there is some meltwater associated with clasts in the debris-laden basal ice, perhaps contributing to scattering.

As the ice goes afloat, the basal fluting and deformed, debris-laden ice are transported from the grounding zone and become the base of the ice shelf (Figure 15). The underlying ocean water provides a stronger reflector than till, but scattering from the complex interface causes the reflector to be weaker than a purely specular contact between ice and seawater. Melting progressively removes the flutes [*Reynolds and Whillans*, 1979] as well as the debris in the basal ice, allowing the interface to eventually transition to a more specular reflector, resulting in brighter radar returns. At the adjacent peninsula, melting is faster than in the deeply recessed, shallow, extensive embayment, so the zone of floating ice with a weak reflector is much narrower at the peninsula.

This picture is complicated further by widespread crevassing and possibly by at least a little brackish water in the upstream areas of the embayment. And because of the odd geometry of the embayment, flow is in some places nearly parallel to the grounding line and in other places more nearly perpendicular, causing complexity in the orientation of crevassing, fluting, etc. relative to our radar survey grid, with considerable effects on the data. Although sufficiently thick freeze-on ice will increase englacial attenuation and decrease basal reflectivity [*MacGregor et al.*, 2011], we cannot rule out the presence of a thin veneer of accretionary ice in downstream regions, which also could smooth the interface and favor more nearly specular reflection without significantly affecting dielectric contrast across the interface. Despite additional complexities introduced into our data from basal crevassing, variable orientation of crevasses and flutes, and perhaps variations in water conductivity and distribution of water flow, we believe that additional studies should start from the hypothesis that grounded ice overlies thawed till. Fluting develops or is amplified in the complex grounding zone through interactions of sedimentation and melting by tidal water flows, and the resulting roughness melts off under the ice shelf, with faster melting near peninsulas rather than in shallow, low-slope embayments (Figure 15).

7.2. Ice-Ocean Interactions

Our radar data suggest significant differences in sediment deposition, geometry, and ice-ocean interactions at two nearby sites of the Whillans Ice Stream grounding zone. Unexpectedly, low basal reflectivity over some floating areas of the embayment may arise at least in part from processes associated with entrained debris in the basal ice and its melt-out, confirming the importance of this mechanism of debris transport [*Christoffersen et al.*, 2010]. Additional sediment transport in deforming subglacial till may still occur. It remains possible that the variations in ice and water pressure associated with tidal flexure, and strengthening of the till through compaction, lead to sediment entrainment to the ice through regelation into the bed or possibly even folding processes [e.g., *Alley et al.*, 1997] before melting out beneath the ice shelf; this would compete with enhanced melting beneath the region of tidal flexure from increased basal shear stress and warmth of sea water pumped inland there. Direct sediment flux in waters from subglacial lake drainage events is likely small, given the relatively low volumes and rates involved, but may transiently be significant during drainage events [*Carter and Fricker*, 2012; *Christianson et al.*, 2012].

Steady state water fluxes from beneath the ice sheet likely are insufficient to support development of a strong buoyant meltwater plume circulation in the subice shelf cavity. The very low ice-bottom and seafloor slopes in the embayment may further limit thermohaline plume formation by extending the zone of tidal mixing farther seaward, as shown by the low tidal elevation anomaly in the embayment (Figure 2a), thus limiting the basal melt rate in this geometrically constrained, tidally mixed zone [*Jenkins and Doake*, 1991; *Holland and Jenkins*, 1999; *Jenkins*, 2011]. Although basal melt rate will increase during subglacial lake drainage episodes, these appear to be too episodic and short duration to compensate for the protection provided by the embayment. During subglacial lake drainage, thermohaline circulation may develop transiently in the embayment in the slightly deeper water of the channel, which may have been formed by enhanced discharge and maintained by tidal as well as thermohaline processes [*Horgan et al.*, 2013b], but the constrained, low-slope environment

would still limit the circulation strength and thus also the melting rate. As a result of this low basal melt rate, sediment deposition in the embayment occurs over a large area, which is manifested as low radar basal reflectivity and very low-slope progradational sediment deposition [*Horgan et al.*, 2013a]. Nonetheless, the low slopes in the embayment mean that the tidal range causes grounding line migration to be larger than in other regions, with shallow water inflow extending long distances. We hypothesize that interactions of this flow with ongoing sedimentation give rise to lobate or ridged sedimentation, channelizing the water flow to localize melting and generate fluting in the ice (Figure 15), which is widespread in the subglacial embayment as indicated by the low basal reflectivity. In deeper water farther offshore, the lack of strong thermohaline circulation and the smaller influence of the deeper bed on water flow allow the fluting to melt off (Figure 15), leading to a flatter and more nearly specular reflector. Our data are suggestive that fluting develops at multiple wavelengths.

Data collected over the subglacial peninsula show low reflectivity extending from grounded ice only a few hundred meters into the ice shelf before a relatively sudden brightening to values typical of smooth ice over seawater. We interpret this as showing that sediment melt-out and deposition are completed in the first few hundred meters seaward of the grounding line [*Horgan et al.*, 2013a]. This is most likely due to a higher basal melt rate in this location, despite a subglacial drainage flux that is very likely lower than that in the embayment and may be close to zero. The tidal anomaly at the subglacial peninsula is much higher (Figure 2b) and the position is inherently more exposed to the ocean, suggesting a more robust thermohaline circulation and thus a higher basal melt rate. As a result of this higher basal melt rate, the area of sediment deposition is much narrower on the peninsula, and sediment is deposited more abruptly, leading to the development of small, but recognizable grounding zone sediment wedges [*Horgan et al.*, 2013a].

These observations suggest that the basal melt rate and the area of melt-out sedimentation in low-slope grounding zones are controlled primarily by exposure to the ocean and tidal currents. Subglacial water flux from grounded ice in both locations is likely low enough that it does not promote a strong thermohaline circulation. Our observations may be generally applicable to West Antarctica's Siple Coast and other low-slope regions, but not to regions of higher flux subglacial drainage or steeper geometries elsewhere. We note, however, that if outburst flooding generates a channel, it may be maintained by tidal flow under some conditions, thus influencing processes well after the outburst flood ends [*Horgan et al.*, 2013b].

7.3. Grounding Zone Stability

Quantitative estimates of sediment and water flux across the ice sheet grounding line are poorly constrained. Our data combined with recent in situ observations and direct sampling from the Whillans Ice Stream grounding zone will significantly improve this picture. Here we present some initial interpretation based solely on the geophysical data. Borehole drillings and initial observations at this location in the 2014–2015 austral summer indicate that there are ~15 m of dirty basal ice, with ~10 to 20% debris content [*Scherer et al.*, 2015]; widespread drilling on grounded ice along the Siple Coast showed at least a few meters of dirty basal ice are common, with drillings from Kamb Ice Stream also containing 10 to 20% debris content by volume [*Engelhardt and Kamb*, 2013]. This debris can supply up to ~3 m of till as it melts out of the ice. The ice in this location moves ~400 m a^{-1}. At the peninsula location, radar basal reflectivity indicates that any sediment melt-out probably occurs within the first 500 m seaward of the grounding line, implying basal melt rates on the order of 10 m a^{-1}. In contrast, reflectivity is reduced over ~5 to 10 km in the embayment, so we infer a much lower basal melt rate of less than ~0.5 m a^{-1}. Even though basal melt rates are higher at the peninsula, its grounding line position may be more stable due to the more spatially focused sedimentation.

The recent deceleration of Whillans Ice Stream [*Joughin et al.*, 2005] is not matched by strong deceleration of other tributaries of the Ross Ice Shelf over the same interval, so "drag" from the ice shelf is expected to be contributing to enhanced longitudinal extension/decreased longitudinal compression near the grounding zone of Whillans, causing thinning there. The rapid sedimentation in the peninsula region may stabilize the grounding line against retreat or even drive progradation. In the embayment, where sediment is deposited more slowly over a larger area, retreat in response to the thinning is much more likely. The thinning ice would easily float off the nearly flat bed, resulting in grounding line retreat, and the opening of a long, thin ice shelf cavity with slow melting because a constrained geometry prevents efficient ingress of ocean currents. Such a process could have formed the embayment we surveyed. This water column is now being gradually filled by sediment, supplied from sediment melting out of the basal ice and any in-wash from subglacial water and sediment flux at the grounding line. These sedimentation processes would result in a very thin, low-profile

grounding zone wedge that would be difficult to recognize as a classic wedge deposit. This setting is thus quite different from the locations that create high-profile wedges that are so well known downstream [*Anderson et al.*, 2002] and that may be presently forming at the nearby peninsula.

Although the current ice shelf cavity may be infilling, the lack of a high-profile grounding zone sediment wedge [*Horgan et al.*, 2013a] in this location could lead to an unstable grounding line in the absence of another stabilization mechanism, especially if the ice stream continues to decelerate. We suggested tidal compaction of subglacial till was one such stabilizing mechanism [*Christianson et al.*, 2013], which requires only the presence of till upstream of grounding, and is indicated by both radar and seismic data. This grounding zone is still not strongly stabilized against retreat and such retreat could occur due to a large increase in subglacial water flux (possibly in response to subglacial lake drainage), an increase in ice shelf cavity water temperature causing higher basal melt rates, or further deceleration of the grounded ice. Future ice sheet models should note that grounding lines in subglacial embayments, even if lacking prominent subglacial channels, are probably especially prone to retreat via changes in subglacial water flux, ice flux, and ocean temperature.

8. Conclusions

We present a comprehensive radar survey of an ice sheet grounding zone. Radar basal reflectivity differs significantly in different areas of our survey. The basal reflectivity inland of grounding is consistent with that expected from an ice-water-saturated till interface, with differences in water conductivity driven by tidal flexure pumping some seawater upglacier of grounding in favorable locations. In the subglacial embayment, basal reflectivity over portions of the floating ice is unexpectedly dim. Our modeling indicates that this is likely the effect of debris melt-out and undulatory ice-bottom topography. Eventually, reflectivity brightens to that expected from an ice-seawater interface. Over the nearby peninsula that is more exposed to ocean currents, basal reflectivity brightens more abruptly, indicating a higher basal melt rate, which leads to more rapid sediment deposition over a smaller area. In both locations, our data indicate that extensive sediment deposition occurs in and just downglacier of grounding zones via melt-out of debris in basal ice [*Christoffersen et al.*, 2010]. Where extensive tidewater flow occurs in shallow water (i.e., the subglacial embayment), we infer that interactions with the sediment being deposited lead to sediment ridges or debris-flow lobes, which may locally be stabilized by compaction when exposed during falling tides, separated by channels melted into the ice by the tidal flow; a range of channel sizes is most consistent with our data.

In the grounding zone, radar returns are complex because of effects associated with off-axis imaging of fluting and/or channelization, and perhaps also of sediment deposits, and sediment melting out. Scattering from englacial debris surrounded by meltwater and from basal roughness associated with melt-out of individual clasts or debris aggregates may contribute to the diffuse basal reflector observed in the upglacier part of the ice shelf in the embayment. We also image numerous large subglacial crevasses, and hyperbolic returns indicate that there may be many small crevasses below the imaging resolution of the radar. Of particular interest is the fact that some of the large crevasses seem to have propagated upglacier as well as upward, perhaps in response to transient basal shear stress during tidal migration of the grounding line.

In summary, there are several important conclusions that arise from our data and modeling: (1) radar reflectivity in the grounding zone is reduced by entrained sediment and basal roughness; (2) sediment deposition via melting of debris-laden basal ice may be more important than sediment flux from the upstream, grounded ice in at least some grounding zones [see also *Christoffersen et al.*, 2010]; and (3) grounding lines in subglacial embayments without vigorous thermohaline circulation lack high-profile sediment wedges and thus are more vulnerable to forcing from the ocean, subglacial water system, or ice dynamics. Thus, modeling studies should focus especially on properly depicting the coupled evolution of the ice shelf geometry and buoyant ocean-plume circulation.

Appendix A: Englacial Attenuation

The power returned from the ice-bed interface (P_r) is a function of the transmitted power (P_t), effective antenna gain (G), ice thickness (H), depth-averaged one-way attenuation length (L_a), and (power) reflectivity of the ice-bed interface [*Bogorodsky et al.*, 1985]:

$$P_r = \frac{P_t G}{4\pi(2H)^2} \exp\left(\frac{-2H}{L_a}\right) R_{ib}, \tag{A1}$$

where we neglect losses due to birefringence and volume scattering, which are small at 5 MHz [*MacGregor et al.*, 2007]. Although we record P_r, the term of interest is R_{ib}, which can be directly interpreted in terms of basal properties (see Table 1). The only other term in equation (A1) that we measure is ice thickness (H), so we cannot calculate R_{ib} directly. Thus, to correct for spherical spreading, englacial radar wave attenuation, and system characteristics, following *MacGregor et al.* [2011], we use the power reflectivity of the first multiple of the basal reflection, which is given by

$$P_{r1} = \frac{P_t G}{4\pi(4H)^2} \exp\left(\frac{-4H}{L_a}\right) R_{ib}^2 R_{fa}, \tag{A2}$$

where R_{fa} is the power reflectivity of the firn-air interface and all other terms are the same as in equation (A1). Taking the ratio of the first multiple of the basal reflection (P_{r1}) to the primary basal reflection (P_r) yields

$$\frac{P_{r1}}{P_r} = \frac{1}{4} \exp\left(\frac{-2H}{L_a}\right) R_{ib} R_{fa}. \tag{A3}$$

Then attenuation length (L_a) is given by a linear least squares fit (constrained to pass through the origin) in log space [*MacGregor et al.*, 2011] or

$$\ln\left(\frac{4}{R_{ib}R_{fa}} \frac{P_{r1}}{P_r}\right) = -\frac{2}{L_a} H. \tag{A4}$$

Depth-averaged attenuation length is converted to depth-averaged attenuation rate (N_a; dB/km) using $N_a = 4343/L_a$ [*Jacobel et al.*, 2009]. Alternatively, equation (A4) can also be used to calculate the attenuation rate for every trace with a detectable primary bed reflection and its first multiple. In addition to detectable bed and multiple reflections, we must also have a priori knowledge of the dielectric properties of the basal interface, which is possible in our survey because roughly half of our survey is on the Ross Ice Shelf (Figure 2). Once the attenuation length and R_{ib} are known for a subset of our data, we can infer $P_t G$ in this subset. If we then assume $P_t G$ and L_a are constant for our survey, we can calculate R_{ib}.

In nearly all radar profiles, the first multiple becomes detectable as the ice goes afloat (Figure 5a and 5b). However, to implement this method we must know R_{ib}; therefore, we choose to determine L_a over areas where the basal reflection is an unambiguous glacier ice-seawater interface. This also maximizes the signal-to-noise ratio of the first multiple of the basal reflection because the signal of interest is higher in amplitude relative to system noise. We identified these areas as having a relatively thick (>6 m) seismically imaged water column, ice that is in full hydrostatic equilibrium, and uniformly bright basal returned power (i.e., mean raw radar returned power of 126.76 dB with a standard deviation of 2.47 dB; compared to mean of 111.84 dB and standard deviation of 7.95 dB for the entire data set). Using these criteria and assuming that the attenuation rate does not vary over our relatively small survey area where the ice is in plug flow and is sourced from the same tributary with minimal differences in accumulated strain, we identified 5925 traces where the basal reflection was unequivocally a glacier ice-seawater interface (Figure 2b). These traces span 17.76 line kilometers where ice thickness varies by 37.6 m. For these traces, using the Fresnel equations, we calculate the basal power reflectivity as that of a glacier ice-seawater interface at 5 MHz or $R_{\mathrm{isw}} = -0.22$ dB, assuming the dielectric constants of ice and seawater at 5 MHz are $\epsilon_i = 3.2 - 0.25i$ [*Peters et al.*, 2005; *MacGregor et al.*, 2011] and $\epsilon_{\mathrm{sw}} = 79.7 - (9.8 \times 10^3)i$ [*Ellison et al.*, 1998], respectively. Again, following *MacGregor et al.* [2011], we assume $R_{fa} = -17 \pm 1.5$ dB.

The lower signal-to-noise ratio of the first multiple reflection due to the longer travel path length introduces an additional difficulty because a clear wavelet associated with the first multiple becomes more difficult to identify, which complicated calculations of power returned. The primary bed reflection is a clear reversed polarity (+/-/+) echo similar to a Ricker wavelet (Figure 5c), as is expected if the permittivity of the subglacial material is greater than that of ice. Thus, we expect the first multiple of the basal reflection to be a normal (relative to the transmitted pulse) polarity (-/+/-) Ricker wavelet-like echo due to another phase reversal when the radar wave reflects off the ice-bed interface a second time. Inspection of the first multiple reflection shows that this wavelet is somewhat more difficult to identify (Figure 5d). In order to assess the importance of accurately determining this wavelet, we calculated reflection power in three different time windows: (1) three half cycles (classic definition), (2) from local minimum to local minimum surrounding the peak amplitude of the reflection (to eliminate spurious changes in inflection associated with low signal-to-noise ratio (SNR) in the multiple reflection), and (3) over a 10-sample window centered on the maximum of the reflection

(to assess the accuracy of the digitizers at finding local extrema and inflection points). Estimating englacial attenuation rate from a robust (L1-norm) least squares fit of the ratio of the primary basal reflection to the first multiple of the basal reflection as a function of depth following equation (A4) gives $N_a = 16.44 \pm 0.06$, 17.78 ± 0.06, and 19.93 ± 0.09 dB/km, respectively, where uncertainties are given by 95th percentile confidence intervals. These uncertainties are unrealistically low due to the large number of points used to constrain the fit. Therefore, we also estimate the attenuation rate for individual traces, which results in $N_a = 16.6 \pm 2.4$, 17.8 ± 2.1, and 20.1 ± 3.4 dB/km, respectively, where uncertainties are given by one standard deviation. These results highlight the point that indiscriminately using least squares fits of power as a function of changing ice thickness can result in poor estimates of uncertainty and that attenuation rate calculations are relatively insensitive (within uncertainty bounds) to time windows we tested. Due to the relatively low SNR of the first multiple reflection, we choose the second definition of power and proceed accordingly in our analysis using a one-way attenuation rate of $N_a = 17.8 \pm 2.1$ dB/km.

Appendix B: Other Factors Affecting Basal Reflectivity

Other factors that can influence englacial attenuation or power returned from the basal interface, such geothermal flux, ice temperature, crystal-fabric orientation (COF), or basal interface specularity [*Matsuoka*, 2009; *Matsuoka et al.*, 2010], are unlikely to significantly alter the patterns in basal reflectivity discussed here. COF has a relatively weak effect on reflectivity (~1 to 5 dB) at single frequencies [*Eisen et al.*, 2007; *Matsuoka et al.*, 2009, 2012]. Following *Matsuoka et al.* [2012], we deem the power reduction due to birefringence from COF alignment as insignificant because the ice thickness to radar wavelength ratio in our survey is small (nearly identical to that reported in *Matsuoka et al.* [2012]). Although systematic reorientation of ice fabric may occur as a result of traversing an area of high basal friction in the grounding zone [*Christianson et al.*, 2013], there is no evidence of downstream crystal reorientation coincident with the transition to uniformly bright conditions further afloat in the embayment. Also, despite a large grounding zone fold, reflectivity at the subglacial peninsula (Figure 9) changes from that characteristic of an ice-till to ice-seawater interface as expected across the grounding zone, indicating that COF likely has negligible influence on reflectivity in our survey. Strain heating can also increase englacial attenuation by raising the temperature of the ice [*Matsuoka et al.*, 2010, 2012]. Here such effects are likely minor as variations in surface strain rates are small in our survey area in the center of the ice stream. Although some strain from enhanced basal friction in the grounding zone that is not captured by satellite data may affect ice at depth [*Christianson et al.*, 2013], the relatively rapid flow of the ice over this feature (a decade or less) likely results in minimal strain heating. Furthermore, the expected pattern of reflectivity from such an effect (most reduced in the grounding zone and then gradually rising downstream) is not observed, and we do not see such a change in reflectivity over the subglacial peninsula (Figure 9) where the highest amplitude folding (and thus heating) occurs. Finally, the effects of such strain heating calculated using a thermomechanical ice sheet model are relatively minor (<2 dB km^{-1} variation in modeled englacial radar attenuation rate as ice traverses a grounding zone) [see *Matsuoka et al.*, 2012] and cannot fully explain the amplitude reflectivity variation observed here. Finally, although geothermal flux can have a significant effect on englacial attenuation rate [*Matsuoka*, 2009], this is not likely to be a significant factor here due to the absence of local geothermal features in our survey area, low likelihood of significant variation in regional geothermal flux over our relatively small survey area, and our calibration of basal reflectivity to an interface with a well-constrained reflectivity over seawater, so that effects of an unknown geothermal flux are irrelevant as the ice is not in direct contact with material that effectively conducts geothermal heat.

Appendix C: Bed Reflectivity Reduction Due To Basal Roughness: Kirchoff Theory

Echoes returned from a rough reflector are reduced in amplitude compared to echoes returned from a smooth reflector because less energy is reflected toward the receiving antenna. Following *Ogilvy* [1991], *Peters et al.* [2005], and *MacGregor et al.* [2013], we use Kirchhoff theory to model the reduction in reflectivity due to roughness (ρ_n) as

$$\rho_n = \exp\left[-\left(\frac{4\pi\xi_{D_1}}{\lambda_{\text{ice}}}\right)^2\right]\left[I_0\left(\frac{8\pi^2\xi^2_{D_1}}{\lambda^2_{\text{ice}}}\right)\right]^2, \tag{C1}$$

where λ_{ice} is the wavelength of the radar wave in ice ($\lambda_{ice} = 33.8$ m at 5 MHz), I_0 is the zero-order modified Bessel function, and ξ_{D_1} is the RMS height. The RMS height is given by

$$\xi_{D_1} = \sqrt{\frac{1}{N-1}\sum_{m=1}^{N}\left(z'_b(x_i) - \bar{z}'_b\right)^2}, \tag{C2}$$

where $z'_b(x)$ is the linearly detrended along-track bed topography, $\bar{z}'_b$ is the mean detrended bed topography over the horizontal range of interest, and N is the number of points in the horizontal range of interest, which is the width corresponding to the first Fresnel zone ($D_1 = \sqrt{2\lambda_{ice}\frac{H}{\sqrt{\epsilon'_{ice}}}} = 168.35$ m for ice of thickness $H = 750$ m) [*Shepard et al.*, 2001; *MacGregor et al.*, 2013].

Reflectivity reduction as a function of RMS height is shown in Figure 14. If RMS heights are below the imaging resolution of the radar system ($\lambda_{ice}/4 = 8.5$ m for 5 MHz), the topographic variation would not be directly detectable but could still affect the power returned from the basal interface. Here that effect could be significant with possible reduction in bed reflectivity of many decibels (Figure 14).

Acknowledgments

This project was funded by the U.S. National Science Foundation (NSF OPP grants 0838854, 0838855, 0838763, and 0838764) and the National Aeronautics and Space Administration (NASA grant NNX12AB69G). We thank Benjamin Petersen and the WISSARD geophysics 2011–2012 team for assistance with the fieldwork. Rebecca Gobel, Benjamin Keisling, and Lauren Snyder assisted with portions of the data processing. NSIDC provided MODIS MOA, DInSAR, and ICESat GLAS data. GPS base station data were obtained from UNAVCO and SOPAC. We thank Eric Rignot, Helen Fricker, and Geir Moholdt for digitization of the grounding zone in DInSAR and ICESat GLAS data. Joseph MacGregor provided dielectric amplitude modeling code. Logistical support was provided by Raytheon Polar Services, Kenn Borek Air, and the New York Air National Guard. Radar and GPS data are archived at the National Snow and Ice Data Center (http://nsidc.org/data/docs/agdc/nsidc0594/index.html).

References

Alley, K. E., T. A. Scambos, M. R. Siegfried, and H. A. Fricker (2016), Impacts of warm water on Antarctic ice shelf stability through basal channel formation, *Nat. Geosci.*, *9*, 290–293, doi:10.1038/ngeo2675.

Alley, R. B., D. D. Blankenship, S. T. Rooney, and C. R. Bentley (1989), Sedimentation beneath ice shelves—The view from Ice Stream B, *Mar. Geol.*, *85*, 101–120.

Alley, R. B., K. M. Cuffey, E. B. Evenson, J. C. Strasser, D. E. Lawson, and G. J. Larson (1997), How glaciers entrain and transport basal sediment: Physical constraints, *Quat. Sci. Rev.*, *16*, 1017–1038.

Alley, R. B., S. Anandakrishnan, T. K. Dupont, B. R. Parizek, and D. Pollard (2007), Effect of sedimentation on ice sheet grounding-line stability, *Science*, *315*, 1838–1841, doi:10.1126/science.1138396.

Anandakrishnan, S., and R. B. Alley (1997), Stagnation of ice stream C, West Antarctica by water piracy, *Geophys. Res. Lett.*, *24*(3), 265–268.

Anandakrishnan, S., G. A. Catania, R. B. Alley, and H. J. Horgan (2007), Discovery of till deposition at the grounding line of Whillans ice stream, *Science*, *315*, 1835–1838, doi:10.1126/science.1138393.

Anderson, J. B., S. S. Shipp, A. L. Lowe, J. S. Wellner, and A. B. Mosola (2002), The Antarctic Ice Sheet during the Last Glacial Maximum and its subsequent retreat history: A review, *Quat. Sci. Rev.*, *21*, 49–70.

Arcone, S. A. (1995), Numerical studies of the radiation patterns of resistively loaded dipoles, *J. Appl. Geophys.*, *33*, 39–52.

Arcone, S. A., V. B. Spikes, and G. S. Hamilton (2006), Phase structure of radar stratigraphic horizons within Antarctic firn, *Ann. Glaciol.*, *41*, 10–16.

Bender, M. L., E. Burgess, R. B. Alley, B. Barnett, and G. D. Clow (2011), On the nature of the dirty ice at the bottom of the GISP2 ice core, *Earth Planet. Sci. Lett.*, *299*(3–4), 466–473, doi:10.1016/j.epsl.2010.09.033.

Bogorodsky, V. V., C. R. Bentley, and S. T. Rooney (1985), *Radioglaciology*, Springer, 1st ed., New York.

Boithias, L. (1987), *Radiowave Propagation*, 1st ed., McGraw-Hill, New York.

Born, M., and E. Wolf (1999), *Principles of Optics*, 7th ed., Cambridge Univ. Press, Cambridge, U. K.

Brunt, K. M., H. A. Fricker, L. Padman, T. A. Scambos, and S. O'Neel (2010), Mapping the grounding zone of the Ross Ice Shelf, Antarctica, using ICESat laser altimetry, *Ann. Glaciol.*, *51*(55), 71–79.

Carter, S. P., and H. A. Fricker (2012), The supply of subglacial meltwater to the grounding line of the Siple Coast, West Antarctica, *Ann. Glaciol.*, *53*(60), 267–280, doi:10.3189/2012AoG60A119.

Carter, S. P., H. A. Fricker, and M. R. Siegfried (2013), Evidence of rapid subglacial water piracy under Whillans Ice Stream, West Antarctica, *J. Glaciol.*, *59*(218), 1147–1162, doi:10.3189/2013JoG13J085.

Catania, G. A., T. A. Neuman, and S. F. Price (2008), Characterizing englacial drainage in the ablation zone of the Greenland ice sheet, *J. Glaciol.*, *54*(187), 567–578.

Chen, G. (1998), GPS kinematics positioning for airborne laser altimetry at Long Valley, California, PhD thesis, Massachusetts Institute of Technology, Cambridge, Mass.

Christianson, K., R. W. Jacobel, H. J. Horgan, S. Anandakrishnan, and R. B. Alley (2012), Subglacial Lake Whillans—Ice-penetrating radar and GPS observations of a shallow active reservoir beneath a West Antarctic ice stream, *Earth Planet. Sci. Lett.*, *331–332*, 237–245, doi:10.1016/j.epsl.2012.03.013.

Christianson, K., B. R. Parizek, R. B. Alley, H. J. Horgan, R. W. Jacobel, S. Anandakrishnan, B. A. Keisling, B. D. Craig, and A. Muto (2013), Ice sheet grounding zone stabilization due to till compaction, *Geophys. Res. Lett.*, *41*, 5406–5411, doi:10.1002/2013GL057447.

Christianson, K., L. E. Peters, R. B. Alley, S. Anandakrishnan, R. W. Jacobel, K. L. Riverman, A. Muto, and B. A. Keisling (2014), Dilatant till facilitates ice-stream flow in northeast Greenland, *Earth Planet. Sci. Lett.*, *401*, 57–69, doi:10.1016/j.epsl.2014.05.060.

Christoffersen, P., S. Tulaczyk, and A. Behar (2010), Basal ice sequences in Antarctic ice stream: Exposure to past hydrologic conditions and a principal model of sediment transfer, *J. Geophys. Res.*, *115*, F03034, doi:10.1029/2009JF001430.

Creyts, T. T., and C. G. Schoof (2009), Drainage through subglacial water sheets, *J. Geophys. Res.*, *114*, F04008, doi:10.1029/2008JF001215.

Depoorter, M. A., J. L. Bamber, J. A. Griggs, J. T. M. Lenaerts, S. R. M. Ligtenberg, M. R. van den Broeke, and G. Moholdt (2014), Calving fluxes and basal melt rates of Antarctic ice shelves, *Nature*, *502*, 89–92, doi:10.1038/nature12567.

Dowdeswell, J. A., and M. G. Fugelli (2012), The seismic architecture and geometry of grounding-zone wedges formed at the marine margins of past ice sheets, *Geol. Soc. Am. Bull.*, *124*(11–12), 1750–1761, doi:10.1130/B30628.1.

Dutrieux, P., D. G. Vaughan, H. F. J. Corr, A. Jenkins, P. R. Holland, I. Joughin, and A. H. Fleming (2013), Pine Island glacier ice shelf melt distributed at kilometre scales, *Cryosphere*, *7*, 1543–1555, doi:10.5194/tc-7-1543-2013.

Eisen, O., I. Hamann, S. Kipfstuhl, D. Steinhage, and F. Wilhelms (2007), Direct evidence for continuous radar reflector originating from changes in crystal-orientation fabric, *Cryosphere*, *1*, 1–10.

Ellison, W., A. Balana, G. Delbos, K. Lamkaouchi, L. Eymard, C. Guillou, and C. Prigent (1998), New permittivity measurements of seawater, *Radio Sci.*, *33*(3), 639–648.
Engelhardt, H., and B. Kamb (2013), Kamb Ice Stream flow history and surge potential, *Ann. Glaciol.*, *54*(63), 287–298, doi:10.3189/2013AoG63A535.
Engheta, N., C. H. Papas, and C. Elachi (1982), Radiation patterns of interfacial dipole antennas, *Radio Sci.*, *17*(6), 1557–1566.
Fricker, H. A., and T. Scambos (2009), Connected subglacial lake activity on lower Mercer and Whillans Ice Streams, West Antarctica, 2003–2008, *J. Glaciol.*, *55*(190), 303–315.
Fricker, H. A., R. Coleman, L. Padman, T. A. Scambos, J. Bohlander, and K. M. Brunt (2009), Mapping the grounding zone of the Amery Ice Shelf, East Antarctica using InSAR, MODIS and ICESat, *Antarct. Sci.*, *21*(5), 515–532, doi:10.1017/S095410200999023X.
Gades, A. M., C. F. Raymond, H. B. Conway, and R. W. Jacobel (2000), Bed properties of Siple Dome and adjacent ice streams, West Antarctica, inferred from radio-echo sounding measurements, *J. Glaciol.*, *46*(152), 88–94.
Gladish, C. V., D. M. Holland, P. R. Holland, and S. F. Price (2012), Ice-shelf basal channels in a coupled ice/ocean model, *J. Glaciol.*, *58*(212), 1227–1244, doi:10.3189/2012JoG12J003.
Glen, J. W., and J. G. Paren (1975), The electrical properties of snow and ice, *J. Glaciol.*, *15*(73), 15–38.
Gray, L., R. Bindschadler, I. Joughin, L. Padman, P. Vornberger, and A. Khananian (2002), RADARSAT interferometry for Antarctic grounding-zone mapping, *Ann. Glaciol.*, *34*, 269–276.
Haran, T. J., J. Bohlander, T. Scambos, T. Painter, and M. Fahnestock (2005), *Modis Mosaic of Antarctica (MOA) Image Map*, National Snow and Ice Data Center. Digital Media, Boulder, Colo.
Hasted, J. B. (1961), The dielectric properties of water, *Prog. Dielectr.*, *3*, 101–149.
Holland, D. M., and A. Jenkins (1999), Modeling thermodynamic ice-ocean interactions at the base of an ice shelf, *J. Phys. Oceanogr.*, *29*, 1787–1800.
Holland, D. M., R. H. Thomas, B. De Young, M. H. Ribergaard, and B. Lyberth (2008), Acceleration of Jakobshavn Isbrae triggered by warm subsurface ocean waters, *Nat. Geosci.*, *1*, 659–664, doi:10.1038/ngeo316.
Horgan, H. J., and S. Anandakrishnan (2006), Static grounding lines and dynamic ice streams: Evidence from the Siple Coast, West Antarctica, *Geophys. Res. Lett.*, *33*, L18502, doi:10.1029/2006GL027091.
Horgan, H. J., S. Anandakrishnan, R. W. Jacobel, K. Christianson, R. B. Alley, D. S. Heeszel, S. Picotti, and J. I. Walter (2012), Subglacial Lake Whillans—Seismic observations of a shallow active reservoir beneath a West Antarctic ice stream, Earth Planet. Sci. Lett., *331–332*, 201–209, doi:10.1016/j.epsl.2012.02.023.
Horgan, H. J., K. Christianson, R. W. Jacobel, S. Anandakrishnan, and R. B. Alley (2013a), Sediment deposition at the modern grounding zone of Whillans Ice Stream, West Antarctica, *Geophys. Res. Lett.*, *40*, 3934–3939, doi:10.1002/grl.50712.
Horgan, H. J., R. B. Alley, K. Christianson, R. W. Jacobel, S. Anandakrishnan, A. Muto, L. H. Beem, and M. R. Siegfried (2013b), Estuaries beneath ice sheets, *Geology*, *41*, 1159–1162, doi:10.1130/G34654.1.
Irving, J., and R. Knight (2006), Numerical modeling of ground-penetrating radar in 2-D using MATLAB, *Comput. Geosci.*, *32*, 1247–1258, doi:10.1016/j.cageo.2005.11.006.
Jacobel, R. W., B. C. Welch, D. Osterhouse, R. Pettersson, and J. A. MacGregor (2009), Spatial variation of radar-derived basal conditions on Kamb Ice Stream, West Antarctica, *Ann. Glaciol.*, *50*(51), 10–16.
Jacobel, R. W., K. E. Lapo, J. R. Stamp, B. W. Youngblood, B. C. Welch, and J. L. Bamber (2010), A comparison of basal reflectivity and ice velocity in East Antarctica, *Cryosphere*, *4*, 447–452, doi:10.5194/tc-4-447-2010.
Jacobel, R. W., K. Christianson, A. C. Wood, K. J. DallaSanta, and R. M. Gobel (2014), Morphology of basal crevasses at the grounding zone of Whillans Ice Stream, West Antarctica, *Ann. Glaciol.*, *55*(67), 57–63, doi:10.3189/2014AoG67A004.
Jenkins, A. (2011), Convection-driven melting near the grounding lines of ice shelves and tidewater glaciers, *J. Phys. Oceanogr.*, *41*, 2279–2294, doi:10.1175/JPO-D-11-03.1.
Jenkins, A., and C. S. M. Doake (1991), Ice-ocean interaction on the Ronne Ice Shelf, Antarctica, *J. Geophys. Res.*, *96*(C1), 791–813.
Jenkins, A., P. Dutrieux, S. S. Jacobs, S. D. McPhail, J. R. Perrett, A. T. Webb, and D. White (2010), Observations beneath Pine Island Glacier in West Antarctica and implications for its retreat, *Nat. Geosci.*, *3*, 468–472, doi:10.1038/ngeo890.
Jezek, K. C. (1984), A modified theory of bottom crevasses used as a means for measuring the buttressing effect of ice shelves on inland ice sheets, *J. Geophys. Res.*, *89*(B3), 1925–1931.
Jezek, K. C., and C. R. Bentley (1983), Field studies of bottom crevasses in the Ross Ice Shelf, *J. Glaciol.*, *29*(101), 118–126.
Joughin, I., et al. (2005), Continued deceleration of Whillans Ice Stream, West Antarctica, *Geophys. Res. Lett.*, *32*, L22501, doi:10.1029/2005GL024319.
Keller, G. V. (1966), Electrical properties of rocks and minerals, in *Handbook of Physical Constants*, edited by S. P. Clark, Geol. Soc. Am., Boulder, Colo.
King, M. (2004), Rigorous GPS data-processing strategies for glaciological applications, *J. Glaciol.*, *50*(171), 601–607.
Langley, K., A. von Deschwanden, J. Kohler, A. Sinisalo, K. Matsuoka, T. Hatterman, A. Humbert, O. A. Nost, and E. Isaksson (2014), Complex network of channels beneath an Antarctic ice shelf, *Geophys. Res. Lett.*, *41*, 1209–1215, doi:10.1002/2013GL058947.
Le Brocq, A. M., et al. (2013), Evidence from ice shelves for channelized meltwater flow beneath the Antarctic Ice Sheet, *Nat. Geosci.*, *6*, 945–948, doi:10.1038/ngeo1977.
Lekarp, F., U. Isacsson, and A. Dawson (2000), State of the art II: Permanent strain response of unbound aggregates, *J. Transport. Eng.*, *126*(1), 76–83, doi:10.1061/(ASCE)0733-947X(2000)126:1(76).
Logan, L., G. Catania, L. Lavier, and E. Choi (2013), A novel method for predicting fracture in floating ice, *J. Glaciol.*, *59*(216), 750–758, doi:10.3189/2013JoG12J210.
Looyenga, H. (1965), Dielectric constants of heterogeneous mixtures, *Physica*, *31*, 401–406.
MacGregor, J. A., D. P. Winebrenner, H. Conway, K. Matsuoka, P. A. Mayewski, and G. D. Clow (2007), Modeling englacial radar attenuation at Siple Dome, West Antarctica, using ice chemistry and temperature data, *J. Geophys. Res.*, *112*, F03008, doi:10.1029/2006JF000717.
MacGregor, J. A., S. Anandakrishnan, G. A. Catania, and D. P. Winebrenner (2011), The grounding zone of the Ross Ice Shelf, West Antarctica, from ice-penetrating radar, *J. Glaciol.*, *57*(205), 1–12.
MacGregor, J. A., G. A. Catania, H. Conway, D. M. Schroeder, I. Joughin, D. A. Young, S. D. Kempf, and D. D. Blankenship (2013), Weak bed control of the eastern shear margin of Thwaites Glacier, West Antarctica, *J. Glaciol.*, *59*(217), 900–912, doi:10.3189/2013JoG13J050.
Marsh, O. J., H. A. Fricker, M. R. Siegfried, K. Christianson, K. W. Nicholls, H. F. J. Corr, and G. Catania (2016), High basal melting forming a channel at the grounding line of Ross Ice Shelf, Antarctica, *Geophys. Res. Lett.*, *43*, 250–255, doi:10.1002/2015GL066612.
Matsuoka, K. (2009), Pitfalls in radar diagnosis of ice sheet bed conditions: Lessons from englacial attenuation models, *Geophys. Res. Lett.*, *38*, L05505, doi:10.1029/2010GL046205.

Matsuoka, K., L. Wilen, S. P. Hurley, and C. F. Raymond (2009), Effects of birefringence within ice sheets on obliquely propagating radio waves, *IEEE Trans. Geosci. Remote Sens.*, *47*(5), 1429–1443, doi:10.1109/TGRS.2008.2005201.

Matsuoka, K., D. Morse, and C. F. Raymond (2010), Estimating englacial radar attenuation using depth profiles of the returned power, central West Antarctica, *J. Geophys. Res.*, *115*, F02012, doi:10.1029/2009JF001496.

Matsuoka, K., D. Power, S. Fujita, and C. F. Raymond (2012), Rapid development of anisotropic ice-crystal-alignment fabrics inferred from englacial radar polarimetry, central West Antarctica, *J. Geophys. Res.*, *117*, F03029, doi:10.1029/2012JF002440.

Millgate, T., P. R. Holland, A. Jenkins, and H. L. Johnson (2013), The effect of basal channels on oceanic ice-shelf melting, *J. Geophys. Res.*, *118*, 6951–6964, doi:10.1002/2013JC009402.

Murray, T., and G. K. C. Clarke (1995), Black-box modeling of the subglacial water system, *J. Geophys. Res.*, *100*(B7), 10,231–10,245.

Muto, A., K. Christianson, H. J. Horgan, S. Anandakrishnan, and R. B. Alley (2013), Bathymetry and geological structures beneath the Ross Ice Shelf at the mouth of Whillans Ice Stream, West Antarctica, modeled from ground-based gravity measurements, *J. Geophys. Res. Solid Earth*, *118*, 4535–4546, doi:10.1002/jgrb.50315.

Neal, C. S. (1979), The dynamics of the Ross Ice Shelf revealed by radio echo sounding, *J. Glaciol.*, *24*(90), 295–307.

Nowicki, S. M. J., and D. J. Wingham (2008), Conditions for a steady ice sheet–ice shelf junction, *Earth Planet. Sci. Lett.*, *265*, 246–255, doi:10.1016/j.epsl.2007.10.018.

Ogilvy, J. A. (1991), *Theory of Wave Scattering From Random Rough Surfaces*, 1st ed., Inst. of Phys. Publ., Bristol, U. K.

Oswald, G. K. A., and S. P. Gogineni (2008), Recovery of subglacial water extent from Greenland radar survey data, *J. Glaciol.*, *54*(184), 94–106.

Parizek, B. R., and R. T. Walker (2010), Implications of initial conditions and ice-ocean coupling for grounding-line evolution, *Earth Planet. Sci. Lett.*, *300*, 351–358, doi:10.1016/j.epsl.2010.10.016.

Parizek, B. R., et al. (2013), Dynamic (in)stability of Thwaites Glacier, West Antarctica, *J. Geophys. Res. Earth Surf.*, *118*, 638–655, doi:10.1002/jgrf.20044.

Peters, M. E., D. D. Blankenship, and D. L. Morse (2005), Analysis techniques for coherent airborne radar sounding: Application to West Antarctic ice streams, *J. Geophys. Res.*, *110*, B06303, doi:10.1029/2004JB003222.

Prtichard, H. D., S. R. M. Ligtenberg, H. A. Fricker, D. G. Vaughan, M. R. van den Broeke, and L. Padman (2012), Antarctic ice sheet loss driven by basal melting of ice shelves, *Nature*, *484*, 502–505, doi:10.1038/nature10968.

Reynolds, R., and I. M. Whillans (1979), Glacial-bed types and their radar-reflection characteristics, *J. Glaciol.*, *23*(89), 439–440.

Rignot, E., J. Mouginot, and B. Scheuchl (2011), Antarctic grounding line mapping from differential satellite radar interferometry, *Geophys. Res. Lett.*, *38*, L10504, doi:10.1029/2011GL047109.

Scherer, R. P., R. D. Powell, J. J. Coenen, T. O. Hodson, R. Puttkammer, and S. M. Tulaczyk (2015), Geological and paleontological results from WISSARD (Whillans Ice Stream Subglacial Access Research Drilling) Project, Abstract C11C-0769 presented at 2015 Fall Meeting, AGU, San Francisco, Calif., 2015 Dec.

Schoof, C. (2007), Ice sheet grounding line dynamics: Steady states, stability, and hysteresis, *J. Geophys. Res.*, *112*, F03S28, doi:10.1029/2006JF000664.

Shepard, M. K., B. A. Campbell, M. H. Bulmer, T. G. Farr, L. R. Gaddis, and J. J. Plaut (2001), The roughness of natural terrain: A planetary and remote sensing perspective, *J. Geophys. Res.*, *106*(E12), 32,777–32,796, doi:10.1029/2000JE001429.

Shreve, R. L. (1972), Movement of water in glaciers, *J. Glaciol.*, *11*(62), 205–214.

Siegfried, M. R., H. A. Fricker, S. P. Carter, and S. Tulaczyk (2016), Episodic ice velocity fluctuations triggerd by a subglacial flood in West Antarctica, *Geophys. Res. Lett.*, *43*, 2640–2648, doi:10.1002/2016GL067758.

Smith, A. M. (1996), Ice shelf basal melting at the grounding line, measured from seismic observations, *J. Geophys. Res.*, *101*(C10), 22,749–22,755.

Smith, B. E., H. A. Fricker, I. R. Joughin, and S. Tulaczyk (2009), An inventory of active subglacial lakes in Antarctica detected by ICESat (2003–2008), *J. Glaciol.*, *55*(192), 573–594.

Smith, B. M. E., and S. Evans (1972), Radio echo sounding: Absorption and scattering by water inclusion and ice lenses, *J. Glaciol.*, *11*(61), 133–146.

Stanton, T. P., W. J. Shaw, M. Truffer, H. F. J. Corr, L. E. Peters, K. L. Riverman, R. Bindschadler, D. M. Holland, and S. Anandakrishnan (2013), Channelized ice melting in the ocean boundary layer beneath Pine Island Glacier, Antarctica, *Science*, *341*, 1236–1239, doi:10.1126/science.1239373.

Ulaby, F. T., R. K. Moore, and A. K. Fung (1982), *Microwave Remote Sensing, Active and Passive*, 2. Radar remote sensing and surface scattering and emission theory, 1st ed., Addison-Wesley, Reading, Mass.

Walker, R. T., T. K. Dupont, D. M. Holland, B. R. Parizek, and R. B. Alley (2009), Initial effects of oceanic warming on a coupled ocean-ice shelf-ice stream system, *Earth Planet. Sci. Lett.*, *287*, 483–487, doi:10.1016/j.epsl.2009.08.032.

Walker, R. T., B. R. Parizek, R. B. Alley, S. Anandakrishnan, K. L. Riverman, and K. Christianson (2013), Ice-shelf tidal flexure and subglacial pressure variations, *Earth Planet. Sci. Lett.*, *361*, 422–428, doi:10.1016/j.epsl.2012.11.008.

Weertman, J. (1974), Stability of the junction of an ice sheet and an ice shelf, *J. Glaciol.*, *13*(67), 3–11.

Welch, B. C., and R. W. Jacobel (2003), Analysis of deep-penetrating radar surveys of West Antartica, US-ITASE 2001, *Geophys. Res. Lett.*, *30*(8), 1444, doi:10.1029/2003GL017210.

Welch, B. C., R. W. Jacobel, and S. A. Arcone (2009), First results from radar profiles collected along the US-ITASE traverse from Taylor Dome to South Pole (2006–2008), *Ann. Glaciol.*, *50*(51), 35–41.

Winberry, J. P., S. Anandakrishnan, R. B. Alley, D. A. Wiens, and M. J. Pratt (2014), Tidal pacing, skipped slips and the slowdown of Whillans Ice Stream, Antarctica, *J. Glaciol.*, *60*(222), 795–807, doi:10.3189/2014JoG14J038.